Diploma Thesis in Informatics

Online Error Correction for the Tracking of Laparoscopic Ultrasound

Tobias Reichl

Technische Universität München
Department of Informatics
Chair for Computer Aided Medical Procedures and Augmented Reality

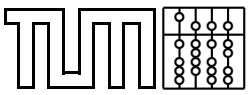

Technische Universität München
Department of Informatics

Diploma Thesis in Informatics

Online Error Correction for the Tracking of Laparoscopic Ultrasound

Tobias Reichl

Director:	Prof. Dr. Nassir Navab
Supervisor:	Dipl. Inf. Marco Feuerstein
	Dipl. Inf. Jörg Traub
Date:	July 16, 2007

Ich versichere, dass ich diese Diplomarbeit selbständig verfasst und nur die angegebenen Quellen und Hilfsmittel verwendet habe.

München, den 16. Juli 2007 Tobias Reichl

Acknowledgments

This work would not have been possible without the work, help, support, and advice of supervisors, colleagues, friends, and family. All achievements of this thesis are also due to them, all errors and omissions are my own.

I would like to thank Dr Nassir Navab for his support during and beyond this diploma thesis. He once told that sharing research is like giving away a part of one's heart. I have ever been impressed by that and tried to live up to the responsibility coming with it.

I would like to thank Oliver Kutter for introducing me to the Chair for Computer Aided Medical Procedures and Augmented Reality of the Technische Universität München and for proof-reading this thesis. Thanks go to Marco Feuerstein for sharing his research with me, half a year of collaboration, and for his patience during various setbacks. Thanks go to Jörg Traub for contributing his ideas to this thesis. Many thanks go to the whole NaNu resp. IFL lab team for their support, especially to Thomas Wendler for his generosity in respect to shared lab equipment.

I would like to thank the German National Merit Foundation for its support during my studies, especially my student adviser Dr Wulf Schiefenhövel for sharing his great enthusiasm with me.

Finally I want to thank my parents Johann and Gabriele and my brother Michael for all their continuous love and support. The most important things in life I learned from them and I won't ever be able to thank them enough. In the same manner, I want to thank my girlfriend Maren for her love and support, for two years now to the day. This thesis would not be what it is now, if she had not always asked the right questions.

Abstract

In abdominal surgery, laparoscopic ultrasound is widely used for minimally invasive procedures. Because of the missing visual feedback, it is often difficult for the surgeons to relate the flexible ultrasound transducer to patient anatomy and images. Utilizing instrument tracking techniques for navigation and augmented visualization can therefore provide great benefits for minimally invasive procedures.

Electromagnetic systems are the only currently available means to determine the pose of the transducer tip inside the patient, its position and orientation. However, the electromagnetic field can be distorted in various ways, leading to erroneous measurements. Different error correction techniques have been developed, but their application to laparoscopic ultrasound is either difficult or they require an additional calibration procedure before each intervention. Additionally, no techniques have yet been proposed for the compensation of dynamic sources of error.

In this thesis two new methods for online error detection and correction for the tracking of flexible laparoscopic ultrasound probes are presented.

The first method utilizes magneto-optic tracking of the ultrasound transducer shaft combined with electromagnetic tracking of the transducer tip. Deviations between optical and electromagnetic tracking of the transducer shaft are used to estimate the distortion of the electromagnetic field at the transducer tip.

The second and more sophisticated method involves a mathematical model of the movements of the flexible transducer tip. All necessary parameters are computed offline in a distortion-free environment and remain valid until the sensors are repositioned. During an intervention the model is fitted to the measurements of the electromagnetic sensor at the transducer tip.

Both methods were rigorously tested in experiments and comprehensively evaluated in comparison to related work. Our results are very promising and especially the model based approach improves the current state of art for both error detection and correction.

Zusammenfassung

Bei minimal-invasiven Eingriffen innerhalb der Bauchhöhle ist der Einsatz von laparoskopischem Ultraschall weit verbreitet. Für Chirurgen ist es wegen der eingeschränken Sicht häufig schwierig, die flexible Ultraschallsonde im Verhältnis zur Anatomie des Patienten und zu anderen Bilddaten einzuordnen. Der Einsatz von Instrumenten-Tracking für Navigation und erweiterte Visualisierung kann daher von großem Nutzen für minimalinvasive Verfahren sein.

Elektromagnetische Systeme sind die einzige heutzutage verfügbare Möglichkeit, die Pose der Sondenspitze im Patienten festzustellen. Das elektromagnetische Feld kann allerdings auf verschiedene Weise verzerrt werden, so dass die Messungen fehlerhaft werden. Unterschiedliche Techniken zur Fehlerkorrektur sind entwickelt worden, ihre Anwendung auf laparoskopischen Ultraschall ist jedoch entweder schwierig oder sie erfordern zusätzliche Kalibrierungsschritte vor jedem Eingriff. Ebenso wurden noch keine Techniken vorgeschlagen, dynamische Fehlerquellen auszugleichen.

In dieser Arbeit werden zwei neue Methoden zur Online-Fehlererkennung und Fehlerkorrektur für das Tracking flexibler laparoskopischer Ultraschallsonden vorgestellt.

Die erste Methode verwendet ein hybrides magneto-optisches Tracking des Sondenschafts, kombiniert mit elektromagnetischem Tracking der Sondenspitze. Die Abweichungen zwischen dem optischen und magnetischen Tracking des Sondenschafts werden dazu verwendet, die Verzerrung des magnetischen Felds an der Sondenspitze abzuschätzen.

Die zweite und weiter entwickelte Methode beinhaltet ein mathematisches Modell für die Bewegungen der flexiblen Sondenspitze. Alle notwendigen Werte werden offline in einer störungsfreien Umgebung berechnet und bleiben so lange gültig, bis die Sensoren neu positioniert werden. Während eines Eingriffs wird das Modell an die Messungen des elektromagnetischen Sensors an der Sondenspitze angepasst.

Beide Methoden wurden gründlich in Experimenten getestet und umfassend im Vergleich zu verwandten Arbeiten ausgewertet. Unsere Ergebnisse sind viel versprechend und insbesondere der modellbasierte Ansatz verbessert den aktuellen Stand der Technik sowohl für Fehlererkennung als auch Fehlerkorrektur.

Contents

Introduction and Related Work

1 Introduction

"It is the business of the physician to know, in the first place, things similar and things dissimilar; those connected with things most important, most easily known, and in anywise known; which are to be seen, touched, and heard; which are to be perceived in the sight, and the touch, and the hearing, and the nose, and the tongue, and the understanding; which are to be known by all the means we know other things." (Hippocrates of Cos, "On The Surgery" [22])

Ever since Hippocrates physicians have striven to know about the inside of the patient's body, in ways as natural and intuitive as possible. Nowadays advanced imaging facilities play a more and more important role in diagnostics and intervention.

Ultrasonography (US) is an appealing technology and one of the most popular imaging modalities, because of its low cost, wide availability, and flexible handling. It provides real time images, it is not invasive and no ionizing radiation has to be administered, and it usually causes only little discomfort for the patient. Additionally it allows the physician to dynamically change the region of interest during the patient examination.

While US in general is still being primarily used for diagnosis, interventional US [23], and especially intraoperative US (IOUS) is becoming more and more popular, e.g. for guidance of needle placement or detection of lesions[1] such as tumors and metastases[2].

Laparoscopic US (LUS) is regularly applied in minimally invasive abdominal surgery for liver, biliary tract, or pancreas [18, 39, 49], e.g. for the staging of hepatic and pancreatic malignancies [14]. In laparoscopic surgery, a camera and surgical instruments are inserted into the patient body through small incisions. Usually video images from inside the patient are displayed on monitors near the operation room table. For some minimally invasive procedures LUS has even become a prerequisite [2]. Minimally invasive procedures are usually favorable compared to open surgery, because patients undergo less trauma, what in turn reduces pain, risk of infections, and hospitalization time.

However, minimally invasive surgery poses additional challenges in terms of restricted movement and due to the limited field of view. Spatial recognition of the transducer's position and orientation and thus of the image plane is difficult especially for novice surgeons. According to Jakimovicz [29], "20 to 40 LUS examinations are necessary to achieve a basic level of experience". Also the value of LUS images is strongly operator dependent.

The limited degrees of positioning the transducer through the trocar[3] access raise difficulties with LUS. The allowable movement of the probe is highly constrained and with the trocar as fixed fulcrum some motions are inverted, some are exaggerated, and overall movement is more complex [14]. The transducer tip needs to be constantly monitored to avoid inadvertent injury of the patient.

[1] Lesions are abnormal tissue usually damaged by trauma or disease.

[2] Metastasis is the spread of a malignant tumor from its primary site to other places in the body.

[3] A trocar is a sharply pointed cylinder through which surgical instruments can be inserted into the patient body. Standard trocar diameters include 11 or 12 mm.

Related Work

Surgeons can be assisted using augmented reality and other technologies to provide navigated US: US images can be displayed in relation to the patient, surgical instruments or preoperative imaging data like from Computed Tomography (CT) or Magnetic Resonance Imaging (MRI). Since endoscopic surgery is essentially a monitor-based surgery, conventional monitor-based augmented reality technologies may be integrated into the surgical work flow straightforward without the need for special display devices or 3D glasses [62].

Ellsmere *et al.* [13, 14], Krücker *et al.* [32], and Estepar *et al.* [15] calibrate LUS to electromagnetic tracking (EMT) and propose an intuitive way to visualize the LUS plane in relation to preoperative CT imaging. This may greatly aid image understanding and identification of anatomical key structures. Kleemann *et al.* [31] use an electromagnetically tracked needle to overlay the needle's position onto the LUS image. Leven *et al.* [35] calibrate LUS to a daVinci surgical robot system to visualize LUS image data directly on the live images of an endoscope.

For instruments with a rigid and non-movable tip optical tracking can be used. An optical tracking body can be attached to the handle outside the patient, so a continuous line of sight can be maintained. However, LUS probes commonly used and preferred by surgeons feature a flexible tip and two-way steering to literally gain more flexibility. With a flexible tip tracking of the shaft is no more sufficient to estimate the tip pose.

Closestly related to the subject of this thesis is the work presented by Sato *et al.* and Nakamoto *et al.* [45, 51, 52], who co-calibrated EMT and optical tracking (OT) for visualization of three-dimensional US. They attach an electromagnetic sensor to the US transducer tip and an optically tracked body to the electromagnetic transmitter. Thus they can determine the pose of the transducer relative to the optical tracking coordinate frame and achieve mobility of the electromagnetic transmitter.

Sato *et al.* [51] use a transducer that is steerable in one direction. They attach an optically tracked body to the transducer shaft outside the patient and calibrate "the plane of the probe tip motion" relatively to this tracking body. During an intervention they combine this constraint with EMT measurements from a system, that can track only five degrees of freedom. Thus they are able to overcome one missing degree of freedom and are able to compute the transducer tip position and orientation in six degrees of freedom.

Other clinical applications include three-dimensional US (3DUS) [19, 44, 46]. Compared to other 3D imaging modalities like CT or MRI, 3DUS is cheap, flexible, and close to clinical routine. Typically a tracking system, e.g. OT or EMT, is used to track the transducer and US data is recorded together with the pose of the tracked transducer. Harms *et al.* [19] use tracked LUS for generation of 3DUS. There exist ideas to estimate the three-dimensional (relative) pose of the US transducer from only the two-dimensional US image data, e.g. by correlating speckles in neighboring US images, as proposed by Tuthill *et al.* [57] and Prager *et al.* [47]. However Li *et al.* [37] found that real freehand 3DUS using only speckle correlation anylsis is not possible.

3DUS supports better image understanding and provides exact measurements of anatomical distances and volumes. Given three-dimensional data, reconstruction of arbitrary slices is possible, even those, which would be impossible to obtain using only a regular transducer [46]. Ideally 3DUS provides all benefits of two-dimensional US.

A serious problem with electromagnetic tracking is that distortions of the electromag-

netic field can lead to erroneous tracking data. Distortions can be caused by ferromagnetic materials or electrically powered devices inside or near the tracking volume, e.g. by surgical instruments, operating room tables or imaging devices like mobile C-arms[4].

Hummel *et al.* [26, 28] and Nafis *et al.* [42] did a thorough evaluation of static EMT position and orientation errors. Required accuracy is application dependent, but tracking errors up to the centimeter scale can occur, what seriously impacts most applications.

Birkfellner *et al.* [3, 5, 6] use a hybrid tracking system, namely a pointer tracked both by EMT and OT, to overcome the drawbacks of either technology and to detect EM field distortions. To compensate static errors caused by stationary objects, various calibration techniques have been proposed: Nakada *et al.* [43] and Wu and Taylor [61] use a hybridly tracked object and they correct position and orientation error using polynomial models. Birkfellner *et al.* [5] and Mucha *et al.* [41] use two sensors, which are fixed in relation to each other, to obtain redundant measurements and use the distance of their two measurements from each other as a plausibility measure.

Kindratenko [30] provides a detailed overview of static EMT position and orientation error correction methods. Chung *et al.* [9] model static position and orientation error as function of both position and orientation using splines[5]. Livingston and State [38] use a look-up table based on position for position and orientation error correction.

Usually a set of well-distributed measurements for all six degrees of freedom (DOF) is obtained together with a set of reference measurements, often based on OT. Then a field distortion function can be constructed based either on look-up tables (up to 3 DOF for parameters and 6 DOF for values) or polynomials (up to 6 DOF for both parameters and values). Although this provides good results, only static and non-moving distortions can be compensated. Also the calibration procedure has to be repeated for every new operating room setup.

Hybrid tracking as proposed by Nakamoto *et al.* [45] also covers dynamic relocation of the EMT transmitter, but again cannot compensate moving sources of error.

Shortcomings of Related Work

There is a clear need for detection and correction of static and dynamic tracking errors. The application of existing error correction techniques to LUS poses additional challenges, because optical tracking is only possible as far as a line of sight can be maintained, which is not possible inside the human body.

Sato *et al.* [51] already presented a simple model of possible transducer tip movements. However, their focus was on obtaining six degrees of freedom for their measurements instead of on error correction, and so they did not exploit tracking redundancy. Furthermore, our transducer features two-way steering, so apart from sharing the same basic idea their approach is not applicable to our case.

In this thesis we present a new approach to online error detection and correction for the tracking of laparoscopic ultrasound. Several methods are introduced, evaluated, and compared. They may be combined to achieve better performance and to improve the state of art.

[4] A C-arm is an X-ray image intensifier, that can be used to image the patient in the operating room.

[5] In mathematics, splines are piecewise polynomial functions, that can be used to interpolate data.

Setup and Methods

2 Setup and Methods

In this chapter the system setup and all necessary calibration steps are described, before we present our proposed methods for online error detection and correction.

Throughout the presented methods we use mathematical techniques like matrix and quaternion arithmetics and linear equation systems. For nonlinear optimization we use the Levenberg-Marquardt algorithm [36, 40]. If needed, please refer to specific literature for an introduction to those.

2.1 System Setup

The following sections provide a detailed overview of the setup we used for development and evaluation.

2.1.1 Laparoscopic Ultrasound

For ultrasonography (US) a transducer produces ultrasound waves directed into the patient's body. Depending on tissue density those waves are scattered and partially reflected back to the transducer. Based on differences in magnitude and delay of returning waves, gray-scale images of anatomical structures can be computed.

Our laparoscopic US (LUS) probe is a "LAP8-4" by Siemens Medical Solutions (Mountain View, CA, USA). It contains a linear array transducer with a frequency range of 4-8 MHz. Its tip is flexible and four-way steerable with two levers at the handle. The probe diameter is 10 mm, so it fits a standard 10 or 12 mm trocar. From previous experiments by Harms *et al.* [19] it is equipped with a MiniBird sensor (Ascension Technology Corporation, see below) embedded into its tip. This sensor is not used for our experiments, but it has to be considered when we place our own sensors at the probe, see below. For LUS imaging the probe is connected to a "SONOLINE Omnia" system by Siemens Medical Solutions, from which analog B-scan[1] images are transmitted to our visualization workstation.

Our US probe is equipped with two electromagnetic tracking (EMT) sensors, one at the flexible tip (called "tip sensor" below) and one at the rigid shaft ("shaft sensor"). The US probe itself contains ferromagnetic materials, especially at the bending region and the shaft. Birkfellner *et al.* [4] already note "that the influence of US scan probes on the accuracy of EMT is governed by their shielding material". We mounted the tip sensor 4 cm away from the bending region. With the shaft sensor we did not have any choice other than mounting it at the shaft, but we placed this sensor some distance (3 cm) away from the bending region, too.

[1] In B-scan mode a linear array of transducers simultaneously scans a plane through the body, that can be viewed as a two-dimensional image on screen, whereas the A-scan technique uses a single transducer to scan along one line.

The MiniBird sensor embedded into the US probe tip contains a ferrite[2] core, which also distorts the magnetic field. As the tip sensor is mounted several centimeters from the MiniBird sensor, this turned out not to cause problems.

The sensors were hot-melt glued to the US probe using a special low temperature system at only 110 °C (UHU LT 110, UHU, Bühl/Baden, Germany), so neither the sensors nor the probe were damaged – the manufacturer states a maximum applicable temperature of 150 °C for the sensors. Even with glued-on sensors the new diameter of the US probe is smaller than 12 mm, so including a sterile cover it still fits a regular trocar. The transducer setup together with both sensors can be seen in figure 2.1.

Figure 2.1: Transducer tip with EMT sensors.

We verified that switching the US probe scan head on or off did not create measurable deviations of the EMT measurements. Hummel *et al.* [27] recognized "slightly higher" distortions while their transducer was switched on, but we did not recognize any similar behavior with our setup.

Orientation errors in the determination of the transformation from the US coordinate frame to the tip EMT sensor frame can result in additional position errors, which increase with the distance of points in the US scan image from the tip EMT sensor frame origin. To minimize those errors, we mounted the sensor in the middle of the transducer array, on the other side of the transducer. We verified that there were no visibly higher errors at this position than anywhere else, using the vendor-supplied "PCIcubes" tool to display the built-in error metric computed by the EMT system.

[2] Ferrites are ferromagnetic, but electrically non-conductive ceramic compound materials made of iron oxides.

Two optical tracking (OT) bodies were fixed to the probe as well. In order not to disturb the electromagnetic field at the probe tip, we used an OT body entirely made of plastic and hot-melt glued it to the tip ("tip body"). The OT body at the probe shaft ("shaft body") is located at the most proximal position, i.e. as near to the handle as possible, to cover the requirements of clinical setups, where only the handle remains visible outside the patient's body and still a line of sight has to be maintained between tracking cameras and OT body. Also we don't want to hinder insertion of the instrument into the patient body. The precaution not to disturb the electromagnetic field needs not be applied to the shaft OT body, because we can keep a fairly high distance to the shaft EMT sensor (in our experiments the distance was 37 cm) and the shaft OT body does not get near the EMT transmitter during regular usage. Therefore we used a standard OT body containing metal parts and affixed it with a metal clamp (BrainLab, Feldkirchen, Germany).

The tip OT body is only used for our own verification purposes and can be removed afterward. With the glued-on tip OT body the US probe obviously no longer fits a trocar. Calibration of the probe tip axis (see section 2.2.5) has to be done before gluing on the tip OT body.

2.1.2 Optical Tracking

We use optical tracking (OT) for determining the pose, i.e. position and orientation, of the laparoscope, the electromagnetic field transmitter, and the ultrasound transducer.

Our system features four ARTtrack2 cameras and a tracking computer running the DTrack tracking software (cameras and software by ART Advanced Realtime Tracking GmbH[3], Weilheim, Germany). Objects are equipped with OT bodies made of either retroreflective[4] spherical markers or stickers.

Each camera in turn emits an infrared light flash at the operating room setting, for which the markers are highly reflective. The markers can then be segmented from the two-dimensional images easily and markers seen by at least two cameras can be triangulated in space [20]. As there are four cameras on the scene, limited occlusions can be tolerated. If at least three markers are rigidly combined to a non-symmetric tracking body, all six degrees of freedom, i.e. position and orientation, can be obtained for that body. The root mean square error for the static accuracy of the system is stated by the manufacturer as 0.4 mm for position and 0.12 degrees for orientation. We are using the optical tracking coordinate frame as the common world frame for our application, as it is used to track the most objects in our setting.

Advantages of optical tracking include high accuracy and immunity to field distortions like they may occur with electromagnetic tracking. On the contrary, it is limited to where a constant line of sight can be maintained, so it can not be used inside the patient body in minimally invasive surgery.

2.1.3 Electromagnetic Tracking

For tracking the ultrasound transducer tip inside the patient body we use an electromagnetic tracking (EMT) system, because it does not need a direct line of sight.

[3] `http://www.ar-tracking.de/`

[4] Retroreflectors reflect light back to the source, regardless of the angle of incidence.

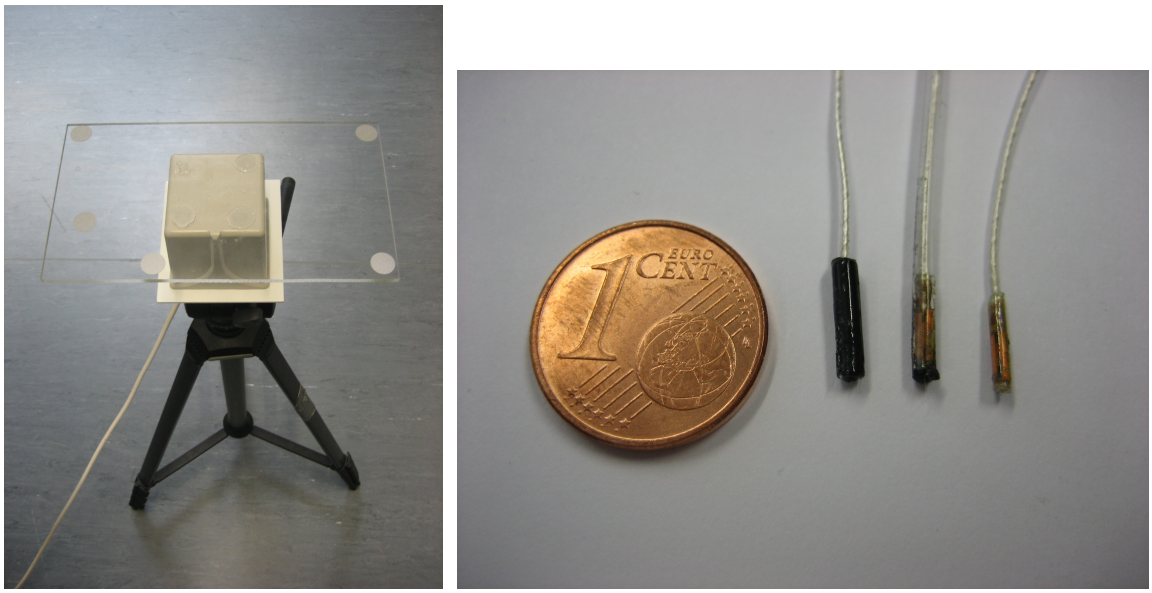

(a) (b)

Figure 2.2: Photo of EMT mid-range transmitter equipped with optical markers (left) and EMT sensors of different size (right). Sensors from right to left: model 130, model 130 with vinyl tubing, model 180.

Our EMT system is a "3D Guidance" unit with model 130 sensors and model 180 sensors, each with and without vinyl tubing. The vinyl tubing is needed for sterilization and provides mechanical protection of the wiring, but for all other purposes it it not a strict requirement. We also use a mid-range transmitter (all by Ascension Technology Corporation[5], Burlington, VT, USA).

In sequence three mutually orthogonal coils in the transmitter create an electromagnetic field of spatially varying intensity. Each time for three mutually orthogonal coils per sensor the current induced by the changing electromagnetic field is measured. From all nine measurements per sensor the pose of the sensor relative to the transducer can be computed. The root mean square error for the static accuracy of the system is stated by the manufacturer as 1.4 mm for position and 0.5 degrees for orientation.

The advantage of electromagnetic tracking is the ability to track sensors without a direct line of sight. Unfortunately the changing magnetic field induces eddy currents[6] in nearby metals or other conductive materials, so the tracking accuracy suffers from field distortions caused by secondary electromagnetic fields. Systems like the 3D Guidance, which are using direct current (DC) instead of alternating current (AC) to generate the electromagnetic field, are able to delay measurements until eddy currents have decayed significantly. However, ferromagnetic materials like iron, nickel or cobalt locally increase the magnetic flux density, and this affects both DC and AC systems. Finally, electrically powered devices can cause additional interferences.

[5] `http://www.ascension-tech.com/`

[6] Eddy currents are currents swirling within conductors, induced by a changing magnetic field. They create magnetic fields, that oppose the effect of the applied magnetic field.

We equipped the EMT transmitter with an optical tracking body ("transmitter body") to allow co-calibration of optical and electromagnetic tracking coordinate frames. To increase the distance between the optical markers and thus to reduce errors in the determination of the body pose, we used a polycarbonate plate as carrier and increased the area covered by the markers.

Determination of the rigid transformation from the EMT coordinate frame to the coordinate frame of the transmitter OT body allows us to move the transmitter freely, because all electromagnetic measurements can then be transformed into the (optical) world frame.

The transmitter was mounted on a stable, yet highly maneuverable stand, like it is normally used for camcorders, using a custom-made plastic connector.

2.1.4 Laparoscope

A laparoscope is an endoscope with a rigid shaft, that can be inserted into the patient's body. Usually laparoscopes feature a "negative element", which widens the angle of viewing and an oblique, i.e. side-looking, optic. Some technical details of the design and optics of a laparoscope are presented in figure 2.3.

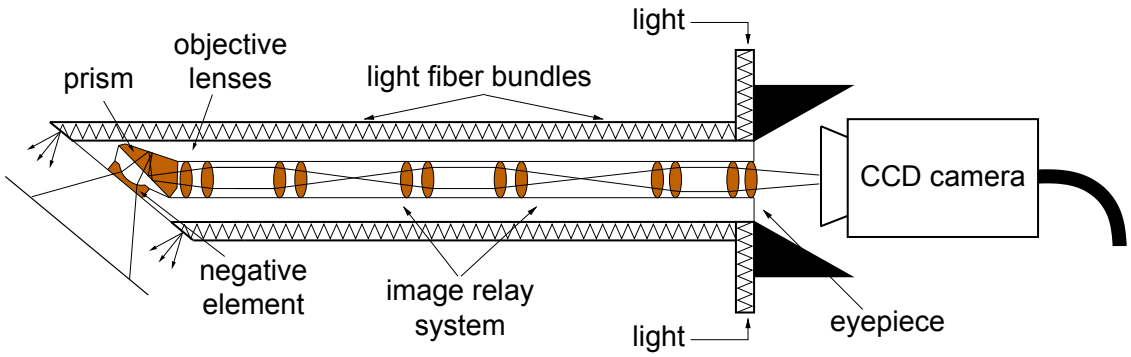

Figure 2.3: Technical details of the design and optics of a laparoscope with an oblique 45° optic. Image courtesy of Feuerstein [16], adapted from Boppart *et al.* [7] and Vogt [58].

We use a laparoscope with a rigid forward-oblique 30° HOPKINS telescope (Karl Storz, Tuttlingen, Germany) like typically used for abdominal surgery. Oblique scopes allow to look behind objects. To separately track the laparoscope camera pose and the rotation of the laparoscope shaft against the camera head two optical tracking bodies were attached to the camera head and the laparoscope shaft. Analog images are taken by a NTSC-based TELECAM one-chip camera and transferred to the visualization workstation.

2.1.5 General Hardware

Real time video data acquisition was done on a standard workstation PC with two "FALCON" frame grabbers (IDS Imaging Development Systems[7], Obersulm, Germany) for the

[7] `www.ids-imaging.com/`

US transducer and camera video, respectively. The workstation is connected to the optical tracking computer by means of Ethernet and to the electromagnetic tracking system by means of Universal Serial Bus (USB). Synchronization of all data streams and visualization was done using the medical augmented reality framework "CAMPAR" [54]. Data streams from all sources are recorded together with their appropriate time stamps, and the framework ensures that at all times matching data is used (for temporal calibration see subsection 2.2.3).

For holding the LUS probe we use a "FISSO" surgical instrument holder (Baitella, Zurich, Switzerland), which contains around ten percent ferromagnetic material. We ensured that at all times this instrument holder was as far away from the EMT system as possible, in order not to distort the electromagnetic field.

All coordinate frames are visualized in figure 2.4.

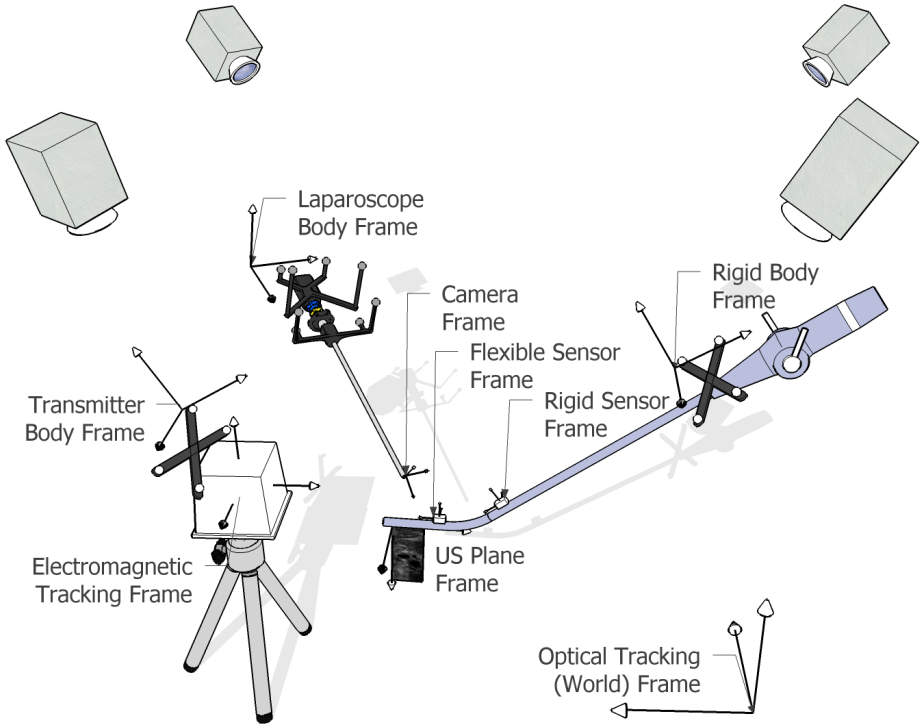

Figure 2.4: Overview of used coordinate frames. The flexible OT body and the Flexible Body Frame have been omitted, as this body is only needed for our accuracy validation, but not in the clinical setup.

2.2 Calibration

Measurements from several different coordinate frames (cf. figure 2.4) have to be transformed into one common world coordinate frame. The optical tracking frame is used to track most objects in our setting, so we use it as world coordinate frame. In total we have to compute the following parameters:

- the transformation from the ultrasound image plane frame to the electromagnetic tip sensor (for US calibration cf. subsection 2.2.1)
- the projection geometry of the laparoscope we use (for camera calibration cf. subsection 2.2.2)
- the delay between measurements from the various systems (for temporal calibration cf. subsection 2.2.3)
- the transformation from the electromagnetic shaft sensor to the shaft optical tracking body and the transformation from the electromagnetic coordinate frame to the transmitter optical tracking body (for hand-eye calibration cf. subsection 2.2.4)
- the transducer tip and shaft axes in the corresponding electromagnetic sensor frame (for axis calibration cf. subsection 2.2.5)

All calibrations can be done offline and remain valid for a long time. They only have to be redone when changes in the setup are made, e.g. a repositioning of sensors and/or markers in respect to tracked objects occurs.

2.2.1 Ultrasonography Calibration

As electromagnetic tracking (EMT) only yields the pose ${}^{EMT}\boldsymbol{T}_{TipS}$ of the tip sensor relative to the EMT transmitter, but not the pose of the US plane, we need to compute the transformation ${}^{TipS}\boldsymbol{T}_{US}$ between those. Coordinates of one point $\boldsymbol{P}_{US}$ in the B-scan image can then be transformed into coordinates $\boldsymbol{P}_{EMT}$ relative to the EMT coordinate frame as

$$\boldsymbol{P}_{EMT} = {}^{EMT}\boldsymbol{T}_{TipS} \cdot {}^{TipS}\boldsymbol{T}_{US} \cdot \boldsymbol{P}_{US}. \tag{2.1}$$

The US coordinates are

$$\boldsymbol{P}_{US} = \begin{bmatrix} s_x \cdot u \\ s_y \cdot v \\ 0 \\ 1 \end{bmatrix} \tag{2.2}$$

where s_x and s_y scale pixel units to millimeters.

We have to consider that any calibration procedure has to be as easy as possible to perform in clinical context, i.e. it has to be user friendly, easy to operate, robust, and fast [50]. As a consequence, user interaction should be kept to a minimum and automation should be used if possible.

Because it does not require the fabrication of a highly specialized calibration phantom we applied "single-wall calibration" as proposed by Prager *et al.* [48]. This involves scanning a planar object ("wall") while moving the US transducer. Instead of scanning the planar bottom of a water bath, as proposed by Prager *et al.*, we use a nylon membrane stretched over a planar frame and submerged into a water bath, as proposed by Langø [34]. The nylon membrane appears as a bright line in the B-scan images and can be further processed.

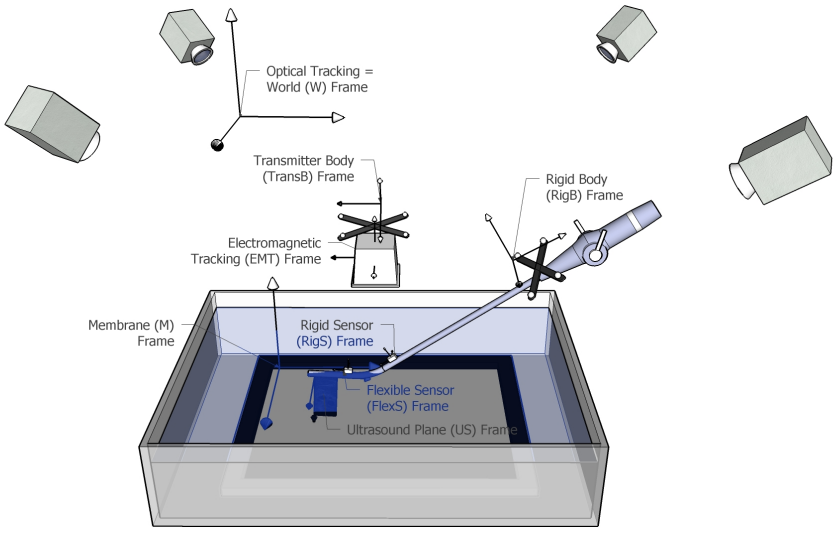

Figure 2.5: Coordinate frames for laparoscopic ultrasound calibration. Image courtesy of Feuerstein [16].

The local coordinate system of the membrane can be defined as aligned with it, such that the z coordinate of the membrane plane is zero. Single-wall calibration builds upon the fact that then for each point $\boldsymbol{P}_M$ of the membrane, which appears in the B-scan image as the point $\boldsymbol{P}_{US}$, one of its three-dimensional coordinates can be set to zero. This yields the following equation for the coordinates of $\boldsymbol{P}_M$:

$$\boldsymbol{P}_M = \begin{bmatrix} x \\ y \\ 0 \\ 1 \end{bmatrix} = {}^{M}\boldsymbol{T}_{EMT} \cdot {}^{EMT}\boldsymbol{T}_{TipS} \cdot {}^{TipS}\boldsymbol{T}_{US} \cdot \boldsymbol{P}_{US} \tag{2.3}$$

The zero component in this equation yields one equation for the determination of the unknown parameters. We can, however, write the equation for up to two pixels of the line. From geometrical observation it can be concluded that 3 parameters cannot be determined: rotation about the z axis and translation within the membrane plane do not affect the z component. Six parameters can be determined for ${}^{EMT}\boldsymbol{T}_{TipS}$ (three for translation and three for rotation), plus the two scaling parameters s_x and s_y. The remaining computable three parameters define the position of the membrane plane in relation to the EMT coordinate frame (contained in ${}^{M}\boldsymbol{T}_{EMT}$) and can be discarded after calibration.

The tracked US transducer is moved through a certain set of poses as proposed by Prager *et al.* [48], to be able to determine all 11 parameters. The required motions are

- vertical translation, i.e. orthogonal to the membrane,
- horizontal translation, i.e. parallel to the membrane in both x and y direction,
- side-to-side rotation, i.e. parallel to the ultrasound scanning direction,
- front-to-back rotation, i.e. orthogonal to ultrasound scanning direction, and

- rotation about the vertical axis.

The bright line of the nylon membrane can be detected in the B-scan images using standard image segmentation techniques [24]. After calibration the position of all pixels in the B-scan image plane can be computed relative to the flexible sensor frame.

For calibration the speed of the US waves has to be recomputed, as it is considerably lower in water at room temperature than it is in average human soft tissue. At 20 °C it is only 1482 m/s, so, if not corrected, structures seen in US images appear farther than they really are [25]. The speed of sound in tap water at 48 °C is 1540 m/s, which most US systems are calibrated for. Tap water at around 48 °C could be kept hot to achieve the same speed of sound, as done by Treece *et al.* [55]. But this distortion can also be corrected for by measuring the water temperature and computing the appropriate speed of sound as proposed by Hsu *et al.* [25], what we opted for.

2.2.2 Camera Calibration

The mathematical model of a camera is a mapping of three-dimensional points in space onto the two-dimensional image plane. We primarily need to determine the parameters of our camera to be able to overlay data onto the laparoscope image. Virtual objects and data can be projected onto the image plane and drawn at their correct positions. Also we want to be able to estimate and to compensate the rather large distortion common for laparoscopes.

One common model is the pinhole camera model as shown in figure 2.6. The projection center is defined by the "camera center" C and this is also the center of the camera coordinate frame. The x axis is perpendicular to the image plane and called the "principal axis". The intersection point of image plane and principal axis defines the "principal point" (x_0, y_0) in image coordinates. The distance between camera center and image plane is the "focal length" f.

Any three-dimensional point $\boldsymbol{X}_C$ in the camera coordinate frame can then be transformed (up to scale) into a two-dimensional point $\boldsymbol{x}_C$ on the image plane by

$$\lambda \begin{bmatrix} \boldsymbol{x}_C \\ 1 \end{bmatrix} = K \cdot \boldsymbol{X}_C \tag{2.4}$$

where K is the "camera calibration matrix"

$$K = \begin{bmatrix} \alpha_x & s & x_0 \\ 0 & \alpha_y & y_0 \\ 0 & 0 & 1 \end{bmatrix} \tag{2.5}$$

and (x_0, y_0) are the coordinates of the principal point, and α_x and α_y define the focal length in image x and y direction respectively (all in pixel units). As a pixel, i.e. a single light-sensor element of the camera chip, needs not be exactly square, the focal length might be different for x and y direction. Together, the coordinates (x_0, y_0) of the principal point and the focal lengths α_x and α_y are the intrinsic parameters of the camera. The "skew parameter" s can safely be set to zero for CCD or CMOS[8] sensors like used for laparoscopes,

[8] "Charge-coupled device" (CCD) and "complementary metal-oxide-semiconductor" (CMOS) are technologies commonly used in the design of light sensors.

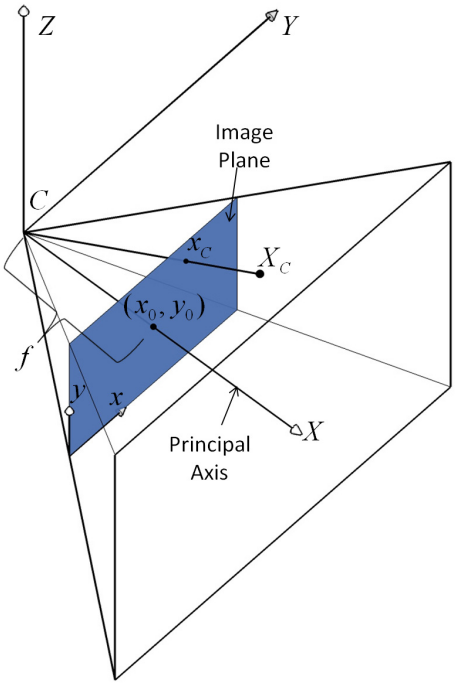

Figure 2.6: Pinhole camera model. Image courtesy of Feuerstein [16].

because their pixels are rectangular.

Hartley and Zisserman [20] present a "Gold Standard Algorithm" for the estimation of an affine camera matrix from world to image point correspondences. We use the methods, that are provided by the Open Source Computer Vision Library[9] (OpenCV) for the determination of the intrinsic parameters of our laparoscope camera, based on Zhang's methods [64] using a simple planar calibration pattern. The inner corners of a checkerboard pattern are automatically detected using OpenCV methods with guaranteed sub-pixel accuracy. Knowing the exact dimensions of the checkerboard pattern (8x7 squares with 10mm side length in our case), the intrinsic parameters can be computed from several poses of the laparoscope while viewing the pattern.

The distortion model employed by the OpenCV implementation for camera calibration is slightly different from Zhang's. In addition to modeling two parameters for the radial distortion, it also determines two parameters for tangential distortion, as proposed by Heikkilä and Silvén [21]. The distortion center for both radial and tangential distortion is assumed to coincide with the principal point. For later automatic undistortion a lookup table is created using OpenCV methods and linear interpolation is usually sufficient to fill the gaps between undistorted point coordinates. For an example of automatic undistortion see figure 2.7.

The extrinsic parameters of the camera, namely location of the camera center and orientation of the camera in respect to the world frame, can be obtained from optical tracking of camera head and laparoscope shaft. Additionally, we need to compute the transformation ${}^{LapB}\boldsymbol{T}_C$ from the camera center to the laparoscope optical tracking body. For this we use

[9] `http://opencvlibrary.sourceforge.net/`

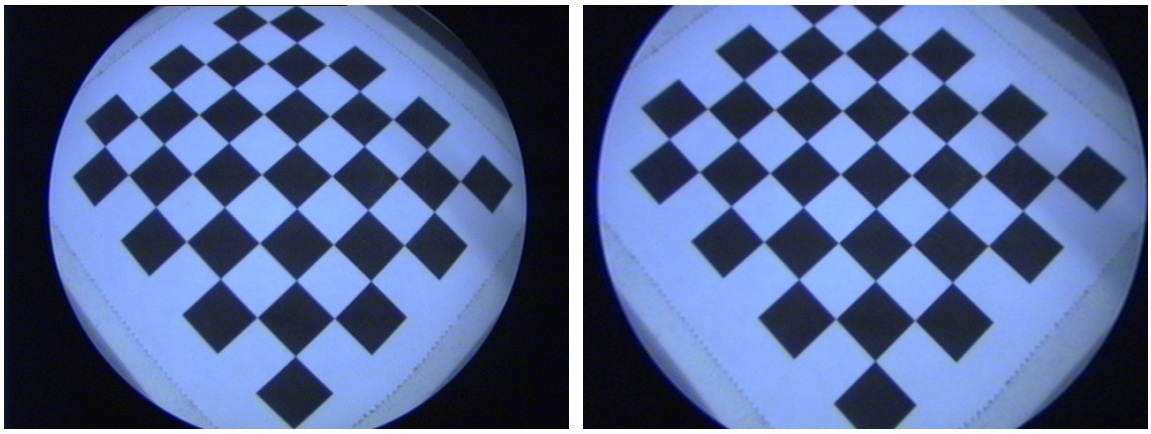

(a) (b)

Figure 2.7: Screenshot of checkerboard camera calibration pattern. Left: original, distorted image. Right: automatically undistorted image after calibration.

a hand-eye calibration approach, similar to the co-calibration of electromagnetic to optical tracking (for hand-eye calibration see 2.2.4).

Special attention has to be paid to the determination of the oblique viewing axis of the laparoscope camera. The transformation ${}^{LapB}\boldsymbol{T}_C$ from the camera center to the laparoscope optical tracking body cannot be assumed to be rigid, because the camera head can be rotated against the laparoscope shaft, which invalidates any rigid transformation. We use the approach suggested by Yamaguchi *et al.* [62] for determining the parameters of the scope rotation axis and the oblique viewing axis. After both axes have been estimated, ${}^{LapB}\boldsymbol{T}_C$ can be computed from the optical tracking of camera head as well as of the laparoscope shaft.

2.2.3 Temporal Calibration

The optical tracking system and our workstation are synchronized to the same reference time, using the Network Time Protocol (NTP). Time stamps for ultrasonography (US) and electromagnetic tracking (EMT) data have to be created when the data arrives at the workstation, because both systems do not automatically provide reliable time stamps at data acquisition time. Thus a more advanced synchronization is required:

Time stamps of EMT data read into the workstation PC and US image data captured by the frame grabber card will have some approximately constant offset to reference time, e.g. resulting from signal processing or traveling time to the workstation. This offset can be determined by a temporal calibration.

Nakada *et al.* [43] propose to minimize the difference in three-dimensional position data for a hybridly tracked object, by varying the temporal offset between OT and co-calibrated EMT. A drawback of this method is that both tracking systems need to be co-calibrated already for temporal calibration, so we opted for a slightly more complex procedure as proposed by Treece *et al.* [55].

The US probe is moved in an approximately linear movement (usually up and down)

while recording both OT and EMT position data. Each collected three-dimensional position data set is reduced using a Principle Component Analysis[10] to get linear values for movement along each main movement component. Linearized data from both tracking systems is normalized and compared, for an example see figure 2.8. The Levenberg-Marquardt algorithm is then used to search for a local minimum of the overall difference. The correlation function is usually well behaved with respect to the temporal offset.

With only minimal changes to the method, namely using the vertical position of the scanned nylon membrane in the US scan image while moving the transducer up and down, the same method can be applied to temporal calibration of US data acquisition.

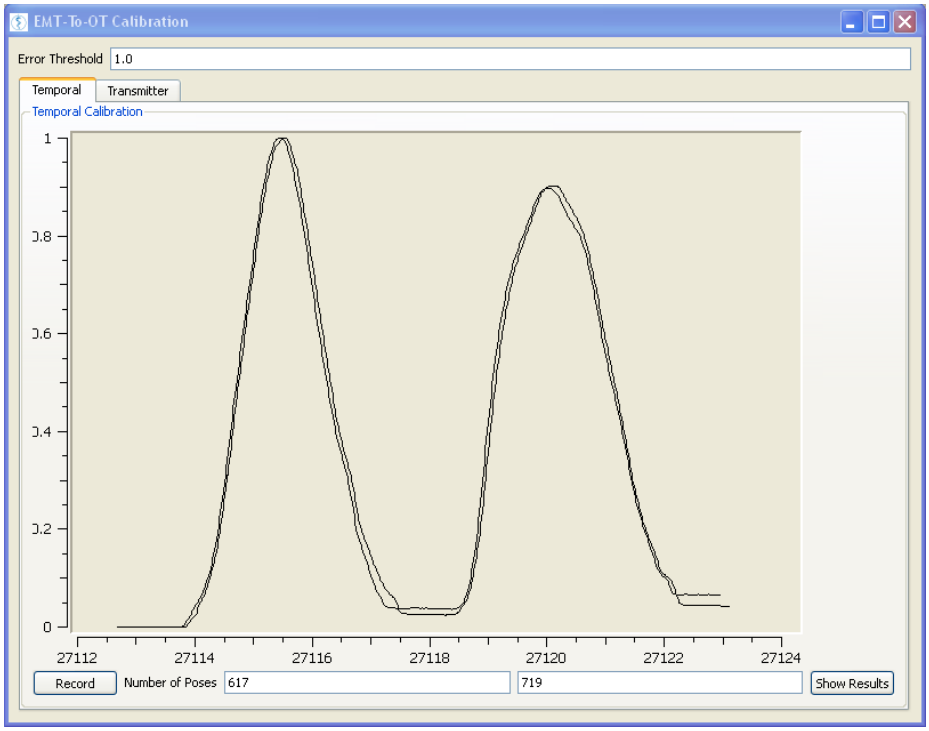

Figure 2.8: Screenshot of user interface with normalized distance data for temporal calibration, already correctly aligned.

2.2.4 Hand-Eye Calibration

We need to transform electromagnetic tracking (EMT) coordinates into the optical tracking (OT) frame, because we use the optical tracking (OT) coordinate frame as world frame. For co-calibration of EMT to OT it is necessary to compute the transformation ${}^{TransB}\boldsymbol{T}_{EMT}$ from the EMT transmitter coordinate frame to the transmitter OT body. Also for both error detection (cf. section 2.4) and error correction techniques (cf. section 2.5) it is necessary to compute the transformation ${}^{ShaftB}\boldsymbol{T}_{ShaftS}$ from the shaft sensor to the shaft OT body. For verification and the "Gold Standard" method we need to determine the transformation

[10] Principle Component Analysis is a mathematical technique to reduce multi-dimensional data sets to lower dimensions for for analysis. It usually involves an eigenvalue decomposition.

${}^{TipB}\boldsymbol{T}_{TipS}$ from the tip sensor to the tip OT body (for a description of the "Gold Standard" method see chapter 3).

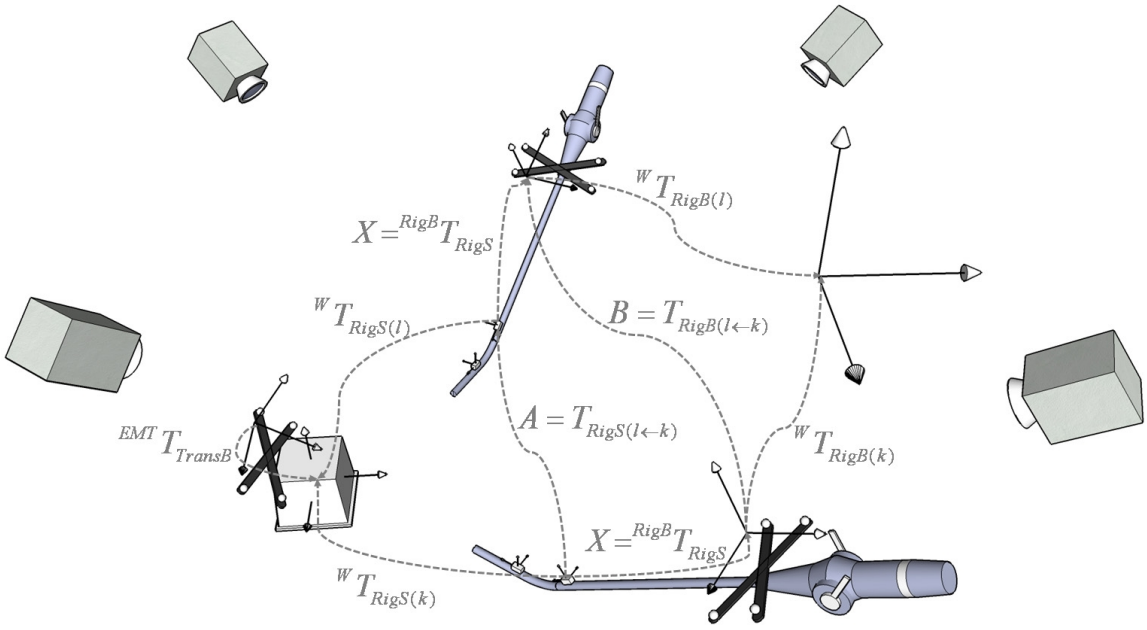

Figure 2.9: Coordinate transformations during magneto-optic hand-eye calibration

All three needed transformations can be computed by performing "hand-eye calibration". This name originates from robotics, where a camera is rigidly fixed to a robot arm and moved around and the transformation between the robot gripper ("hand") and the camera center ("eye") needs to be determined.

Generally speaking, we want to compute the rigid transformation between two objects, whose position can be determined independently by two different tracking systems. Also this computation has to be done without prior co-calibration of both tracking systems – actually, we want to use hand-eye calibration for co-calibration of the tracking systems.

The main idea behind hand-eye calibration is visualized in figure 2.9. When moving the probe from a pose k to a pose l we may define the "hand" motion $\boldsymbol{T}_{ShaftB(l\leftarrow k)}$ and the "eye" motion $\boldsymbol{T}_{ShaftS(l\leftarrow k)}$ between the two poses as

$$\boldsymbol{T}_{ShaftB(l\leftarrow k)} \;=\; \left({}^{OT}\boldsymbol{T}_{ShaftB(l)}\right)^{-1} \cdot {}^{OT}\boldsymbol{T}_{ShaftB(k)} \tag{2.6}$$

$$\boldsymbol{T}_{ShaftS(l\leftarrow k)} \;=\; \left({}^{EMT}\boldsymbol{T}_{ShaftS(l)}\right)^{-1} \cdot {}^{EMT}\boldsymbol{T}_{ShaftS(k)} \tag{2.7}$$

Then the following holds:

$$\boldsymbol{T}_{ShaftB(l\leftarrow k)} \cdot {}^{ShaftB}\boldsymbol{T}_{ShaftS} \;=\; {}^{ShaftB}\boldsymbol{T}_{ShaftS} \cdot \boldsymbol{T}_{ShaftS(l\leftarrow k)} \tag{2.8}$$

To point out how to continue we may substitute $\boldsymbol{T}_{ShaftB(l\leftarrow k)} = A$, $\boldsymbol{T}_{ShaftS(l\leftarrow k)} = B$ and ${}^{ShaftB}\boldsymbol{T}_{ShaftS} = X$ to get

$$A\,X \;=\; X\,B. \tag{2.9}$$

Thus each motion yields three equations and six variables (three each for rotation and translation in ${}^{ShaftB}\boldsymbol{T}_{ShaftS}$) for each motion, so we need at least two motions to be able to solve equation 2.8. To avoid degenerate cases where the rotation angle for one of the motions is too small, we ensure a minimum rotation distance between poses.

The US probe is moved to several poses and the poses of electromagnetic sensors and optical tracking bodies in their respective coordinate frames are recorded. For all possible pairs of recorded poses, the motion between both poses is computed, for electromagnetic tracking as well as for optical tracking. For solving this system of equations we either use the methods of Tsai and Lenz [56] or Daniilidis [11].

For simplicity we assumed that the EMT transmitter does not move during calibration, and so the transformation between both tracking coordinate frames stays fixed (a requirement for hand-eye calibration). This was ensured by a constant monitoring of the transmitter OT body pose. If the movement of that body, and thus the transmitter, was greater than a certain threshold, in our case 0.4 mm, a warning was issued. If the OT tracking data for the transmitter body was used, then the hand motion (cf. equation 2.6) could be defined as

$$\boldsymbol{T}_{ShaftB(l\leftarrow k)} = \left({}^{OT}\boldsymbol{T}_{TransB(l)}{}^{-1} \cdot {}^{OT}\boldsymbol{T}_{ShaftB(l)}\right)^{-1} \cdot {}^{OT}\boldsymbol{T}_{TransB(k)}{}^{-1} \cdot {}^{OT}\boldsymbol{T}_{ShaftB(k)} \tag{2.10}$$

and the EMT transmitter could also be moved during calibration. However, we opted against this, as it would have introduced additional tracking errors from the OT system.

For too small rotations between two poses the rotation axis might not be well-defined [53], so we ensured that all inter-pose rotations had an angle above a certain threshold (we used 23° in our setup).

As stated by Tsai and Lenz [56]

- rotation errors in the determined transformation increase with decreasing rotation angles between poses used for calibration,
- rotation and translation errors increase with decreasing angles between inter-pose rotation axes, and
- translation errors increase with increasing translation between hand (OT) poses.

Whereas we can select poses to maximize inter-pose rotation angles and the angle between inter-pose rotation axes, the probe has to be rotated around the EMT working volume, so especially the translation of the shaft OT body cannot be avoided.

Optimization

There are two possibilities for computing the pose of the shaft EMT sensor in respect to the world (OT) frame: we may either use the pose as measured via EMT, transmitter calibration and OT

$$ {}^{OT}\boldsymbol{T}_{ShaftS} \;=\; {}^{OT}\boldsymbol{T}_{TransB} \;\cdot\; {}^{TransB}\boldsymbol{T}_{EMT} \;\cdot\; {}^{EMT}\boldsymbol{T}_{ShaftS} \tag{2.11} $$

or we may use the pose as computed via hand-eye calibration and OT:

$$ {}^{OT}\boldsymbol{T}_{ShaftS} \;=\; {}^{OT}\boldsymbol{T}_{ShaftB} \;\cdot\; {}^{ShaftB}\boldsymbol{T}_{ShaftS} \tag{2.12} $$

After initial hand-eye calibration the resulting transformations ${}^{TransB}\boldsymbol{T}_{EMT}$ and ${}^{ShaftB}\boldsymbol{T}_{ShaftS}$ are optimized for a per-station minimum translation $\vec{t}_\delta$ and rotation angle α_δ between those two poses, using the Levenberg-Marquardt algorithm.

The functional used for optimization was

$$ \delta = \left\| \vec{t}_\delta \right\| \;+\; 3 \cdot \frac{180}{\pi} \cdot \arccos\left(\frac{\operatorname{trace}\left(\mathrm{R}_\delta\right) - 1}{2} \right). \tag{2.13} $$

We weighted position errors in millimeters to orientation errors in degrees in the ratio of 1:3, approximately reflecting the ratio of root mean square errors, that are stated by the EMT and OT manufacturers for their systems (cf. subsections 2.1.2 and 2.1.3).

Transmitter Calibration

In the same way we can compute the transformation ${}^{TransB}\boldsymbol{T}_{EMT}$ from the EMT coordinate frame to the transmitter OT body. Defining hand motion as

$$ \boldsymbol{T}_{EMT(l \leftarrow k)} \;=\; {}^{EMT}\boldsymbol{T}_{ShaftS(l)} \cdot \left({}^{EMT}\boldsymbol{T}_{ShaftS(k)} \right)^{-1} \tag{2.14} $$

and eye motion as

$$ \boldsymbol{T}_{TransB(l \leftarrow k)} \;=\; \left[\left({}^{OT}\boldsymbol{T}_{TransB(l)} \right)^{-1} {}^{OT}\boldsymbol{T}_{ShaftB(l)} \right]^{-1} \left[\left({}^{OT}\boldsymbol{T}_{TransB(k)} \right)^{-1} {}^{OT}\boldsymbol{T}_{ShaftB(k)} \right] \tag{2.15} $$

we can rewrite equation 2.8 as follows

$$ \boldsymbol{T}_{TransB(l \leftarrow k)} \cdot {}^{TransB}\boldsymbol{T}_{EMT} \;=\; {}^{TransB}\boldsymbol{T}_{EMT} \cdot \boldsymbol{T}_{EMT(l \leftarrow k)} \tag{2.16} $$

and again substitute $\boldsymbol{T}_{TransB(l \leftarrow k)} = A$, $\boldsymbol{T}_{EMT(l \leftarrow k)} = B$ and ${}^{TransB}\boldsymbol{T}_{EMT} = X$ to get

$$ A\,X \;=\; X\,B. \tag{2.17} $$

This can the be solved in the same way as above.

2.2.5 Axis Calibration

For modeling the transducer tip movement (for modeling cf. section 2.3) it is necessary to determine the transducer axes, i.e. tip and shaft axis, each in relation to the respective sensor.

We used a milling cutter to create a calibration phantom in the form of a plastic cylinder, which tightly fits the probe, with a recess for the sensor glued to the probe and a hole at one end to insert an additional EMT sensor, which is used for calibration (“calibration sensor”) .

Note that the tip optical tracking body must not be glued onto the tip before the axis calibration is done, because then the calibration phantom does not fit over the probe any more.

Figure 2.10: Axis calibration phantom, slid over the probe tip. Note the calibration sensor in a small hole at the left.

Calibration of the tip axis is done as follows (analogous for the shaft axis): the calibration phantom is equipped with the "calibration sensor" and slid over the US probe tip (cf. figure 2.10). The phantom is then rotated around the probe (cf. figure 2.11) and the measured position of the calibration sensor is transformed into the tip sensor coordinate frame. At regular intervals this relative position is stored, so we collect a ring-shaped point cloud of measurements. Then the calibration phantom is reversed, fit over the tip sensor, and again rotated around the probe. Because the hole is now at the other end of the calibration phantom, we can now collect points at the other side of the sensor, i.e. a second ring-shaped point cloud. All recorded points have the same distance to the instrument axis, so all of them lie on a cylinder surface.

After ring-shaped point clouds at both sides of the sensor have been collected, a cylinder with radius r around the transducer axis is fitted to our m measurements $\boldsymbol{X}_i, i = 1 \dots m$. The transducer axis is defined by the point b on the axis closest to the sensor and by a unit vector d pointing along it in distal direction, i.e. towards the tip. The sensor's main axis is assumed to point approximately in this direction, so no manual input is needed for computation here. The distance $a(\boldsymbol{X}_i)$ of each measured position from the transducer axis can be computed as

$$a(\boldsymbol{X}_i) = \|d \times (b - \boldsymbol{X}_i)\| \,. \tag{2.18}$$

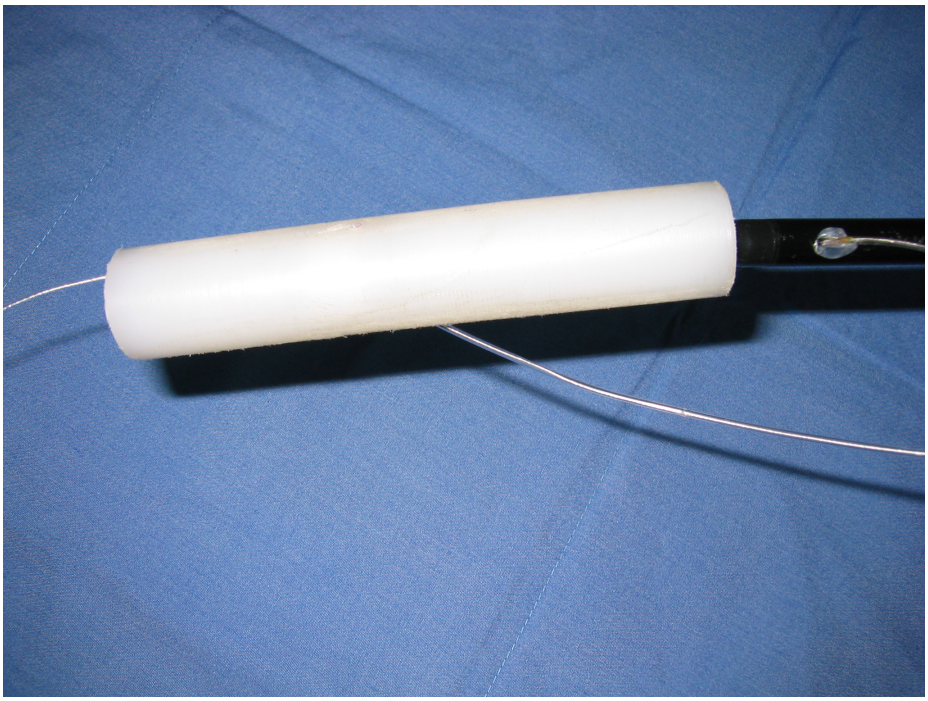

Figure 2.11: Axis calibration phantom, halfway rotated around the probe tip. The tip sensor fits into a recess milled at the inside.

The deviation from the cylinder radius

$$|r - a(\boldsymbol{X}_i)| \tag{2.19}$$

is minimized for all measurements using the Levenberg-Marquardt algorithm. The resulting best b_{Tip} and d_{Tip} define the tip axis and b_{Shaft} and d_{Shaft} define the shaft axis, respectively.

2.3 Modeling

Distortions of the electromagnetic field can introduce errors for all six degrees of freedom. The movement of the transducer's tip, however, has mainly two degrees of freedom, i.e. horizontal and vertical bending controlled by the two steering levers. Modeling the transducer tip movement has the possibility of exploiting the redundancy contained in four degrees of freedom and thus compensate for erroneous tracking. Similarly, deviations from the possible motions can be used to predict erroneous tracking.

The ultrasound transducer does not contain one single joint, but a lengthy bending region extending over approximately three centimeters. This region consists of several short links. In many commercially available laparoscopic instruments 12 links or similar numbers are used, so we assumed the same for our model. Those links alternatingly allow manual horizontal or vertical movement, controlled by one steering lever for horizontal movement and one for vertical movement (see figure 2.12). Each lever offers seven posi-

tions, giving 49 manually selectable tip poses. Due to hardware limitations not every pose is actually reachable.

Figure 2.12: Transducer bending region. The single links allow either horizontal or vertical movement, the overall bending angles are controlled by pulling the cables, pairwise for either direction.

As the tip yields to external pressure as well, continuous motions on an ellipsoid-like surface are modeled to approximate all possible tip poses, i.e. poses of the tip sensor in relation to the shaft sensor. A chain of transformations from the shaft sensor frame to the tip sensor frame is proposed, which is visualized in figure 2.13.

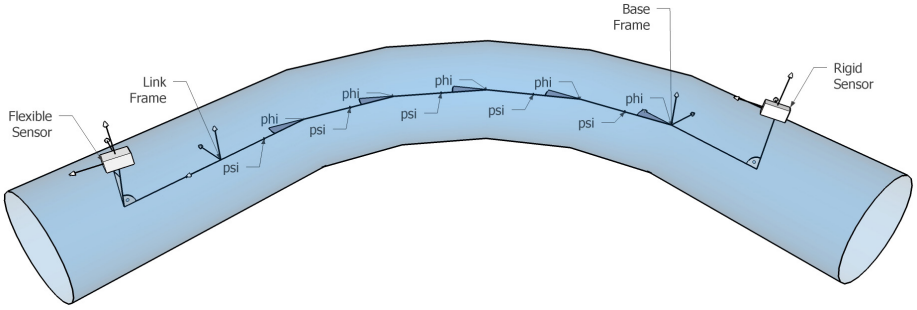

Figure 2.13: Mathematical model of the tip of the flexible ultrasound transducer – only the rotation ϕ about the x axis is visualized here, the rotation ψ about the y axis is zero.

The proposed model is built relatively to the shaft sensor. When it is later used for error detection or correction, the model can be anchored relatively to the shaft optical tracking body, as the transformation ${}^{ShaftB}\boldsymbol{T}_{ShaftS}$ is known from hand-eye calibration (cf. subsection 2.2.4). This avoids additional errors as the the shaft sensor itself might be influenced by distortions as well.

At first, the shaft sensor's coordinate frame is rotated and translated into the "base frame" in such a way that the z axis of the base frame points along the transducer axis. The corresponding transformation ${}^{ShaftS}\boldsymbol{T}_{Base}$ has five degrees of freedom (DOF), i.e. two DOF of rotation to align the sensor with the transducer axis, two DOF of translation onto the axis and another translation along the axis. In particular we do not fix the rotation about the z axis, as it is dependent on the orientation of the sensor. We could fix that rotation by introducing the assumption that the sensor is always mounted at the top side of the shaft, but we decided against it, because this assumption might not be valid.

Starting at the base frame, i.e. the bending region origin, there are n short links, approximating the possible movement. In an alternating manner, each link rotates the transducer axis either ϕ degrees about the x axis or ψ degrees about the y axis, respectively. No rotation about the z axis is assumed, but each link introduces a position offset t_z along the z axis, so in total ${}^{Base}\boldsymbol{T}_{Link}$ has four DOF.

$$ {}^{Base}\boldsymbol{T}_{Link} = \underbrace{\boldsymbol{T}_{Link}(\phi) \cdot \boldsymbol{T}_{Link}(\psi) \cdot \boldsymbol{T}_{Link}(\phi) \cdot \ldots}_{\text{n transformations}} \tag{2.20} $$

where

$$ \boldsymbol{T}_{Link}(\phi) = \begin{bmatrix} 1 & 0 & 0 & 0 \\ 0 & \cos(\phi) & -\sin(\phi) & 0 \\ 0 & \sin(\phi) & \cos(\phi) & t_z \\ 0 & 0 & 0 & 1 \end{bmatrix} \tag{2.21} $$

$$ \boldsymbol{T}_{Link}(\psi) = \begin{bmatrix} \cos(\psi) & 0 & \sin(\psi) & 0 \\ 0 & 1 & 0 & 0 \\ -\sin(\psi) & 0 & \cos(\psi) & t_z \\ 0 & 0 & 0 & 1 \end{bmatrix} \tag{2.22} $$

After the bending region, a final translation and rotation is necessary to align the coordinate frame with the tip sensor. The corresponding transformation is ${}^{Link}\boldsymbol{T}_{TipS}$, which has six DOF. ${}^{Link}\boldsymbol{T}_{TipS}$ has one more DOF than ${}^{ShaftS}\boldsymbol{T}_{Base}$, namely the additional rotation about the transducer axis.

One degree of freedom is "missing" in ${}^{ShaftS}\boldsymbol{T}_{Base}$, because we cannot predict the orientation of the sensor relative to the shaft axis. However, it can be compensated for by choosing other combinations for the angles ϕ and ψ. The difference caused by the alternating sequence of horizontally and vertically steerable links should be negligible. In future work horizontally and vertically steerable links might be replaced by a single link type offering movement in both directions without loosing too much accuracy. On the other hand, one rotation about the z axis is needed, because both sensors can be mounted at different angles relative to the transducer axis, i.e. the tip sensor's position could be rotated about the transducer axis against the shaft sensor's position. The complete transformation from coordinates $\boldsymbol{P}_{TipS}$ in the tip sensor coordinate frame to coordinates $\boldsymbol{P}_{ShaftS}$ in the shaft sensor coordinate frame can be described as

$$ \boldsymbol{P}_{ShaftS} = {}^{ShaftS}\boldsymbol{T}_{Base} \cdot {}^{Base}\boldsymbol{T}_{Link} \cdot {}^{Link}\boldsymbol{T}_{TipS} \cdot \boldsymbol{P}_{TipS} \tag{2.23} $$

All parameters except angles ϕ and ψ remain constant for a given configuration and can be computed offline: After shaft and tip axis have been determined (cf. subsection 2.2.5), in a second step the translation along the shaft axis (contained in ${}^{ShaftS}\boldsymbol{T}_{Base}$), the length of the bending region ($n \cdot t_z$), the number n of links in the bending region, and the angle of rotation about the tip axis and the length of translation along the tip axis (both contained in ${}^{Link}\boldsymbol{T}_{TipS}$) can be estimated.

For every selectable position of the two control levers the relative pose of the tip sensor to the shaft sensor is recorded in a distortion-free environment. Then the model parameters

are optimized numerically using the Levenberg-Marquardt algorithm. The model parameters have to be computed only once, when the electromagnetic sensors are attached to the transducer or when their configuration is changed.

At run-time only two degrees of freedom, i.e. the angles ϕ and ψ, remain to be computed, because they depend on the control levers' positions and external forces affecting the probe tip. They can be optimized numerically, minimizing either the translation to the tip sensor, rotation difference to the tip sensor, or a combination of both. In our experiments we used a weighting of translation in millimeters to rotation in degrees of 1:3, for results and a discussion see section 3.5.

2.4 Error Detection

Every error correction approach using a hybridly tracked object, e.g. as proposed by Nakada *et al.* [43] or Wu and Taylor [61] can trivially be used for error detection. However, it is not possible to redundantly track the transducer tip, but only the transducer shaft. Also we cannot use any distortion function, computed either offline or online, to compare measurements with, because that would not be able to detect dynamic sources of error. Common to all those error detection methods is, they rely on one offline determined transformation resp. distance and monitor deviations from it during an intervention.

Our shaft sensor based method builds upon the fact that optical tracking is not affected by field distortions: Provided that the transformation ${}^{ShaftB}\boldsymbol{T}_{ShaftS}$ from the shaft sensor to the shaft optical tracking (OT) body and the transformation ${}^{TransB}\boldsymbol{T}_{EMT}$ from the electromagnetic tracking (EMT) coordinate frame to the transmitter OT body have been calibrated, there exist two possibilities to determine the position of the shaft EMT sensor in OT coordinates:

1. We may take EMT measurements of the sensor's position relative to the EMT transmitter. Then we use the previously determined transformation ${}^{TransB}\boldsymbol{T}_{EMT}$ from the EMT coordinate frame to the transmitter OT body and optical tracking of the transmitter OT body to transform the sensor's coordinates into the OT coordinate frame (cf. equation 2.11, page 23).

2. The transformation ${}^{ShaftB}\boldsymbol{T}_{ShaftS}$ determines the position of the shaft EMT sensor relative to the shaft OT body. We may use this and optical tracking of the OT body to transform the sensor's coordinates into the OT coordinate frame (cf. equation 2.12, page 23).

In an ideal and error-free setting there should be no difference between those two possibilities. We can, however, determine the difference between those two possibilities to assess the electromagnetic field distortion. Birkfellner *et al.* [5] and Mucha *et al.* [41] use two relatively fixed EMT sensors and the deviation of their distance to detect field distortions. In a similar manner we can provide an alert to surgical staff when the deviation gets too high.

At any time we are able to compute the transformation between the rigid sensor pose as computed via hand-eye calibration and OT ("calibrated pose") and as measured via EMT, transmitter calibration and OT ("measured pose"). Either the translation or the rotation

between both poses, or a combination of both, can be used as a plausibility value with a selectable threshold, when to reject tip sensor data as probably distorted. This method is called "shaft sensor based error prediction" below.

Also, after optimizing the model angles ϕ and ψ, we may compute the remaining distance between the modeled tip sensor position and the uncorrected tip sensor position. With a perfect model in an error-free environment it would always be possible to find model angles ϕ and ψ, such that the modeled tip sensor pose is identical to the uncorrected tip sensor pose. A deviation between those can also be used as a plausibility value. This method is called "model based error prediction" below.

Whenever an error is predicted, the colored frame around the ultrasound plane can be colored red instead of green for prediction of a correct measurement. When using error correction we suggest using a yellow frame.

2.5 Error Correction

We will propose three different methods for (partially) correcting the tracking resp. overlay error. The shaft sensor based approach and the model based approach can be applied to three-dimensional tracking data, the segmentation based approach can be used with live video images.

2.5.1 Shaft Sensor Based Approach

As long as the main error component measured at both sensors is the same, it might be partially corrected: We can compute the distortion of the shaft sensor measurements ${}^{EMT}\boldsymbol{T}_{ShaftS}$ and undo this distortion at the tip sensor. As both sensors can be rotated against each other we have to compute the distortion relative to the world (optical tracking) coordinate frame. We can compute an approximate correction for the distorted pose of the electromagnetic (EMT) tip sensor ${}^{EMT}\boldsymbol{T}_{TipS}$: We separately apply the inverse rotation and translation components of the (shaft EMT sensor) distortion to the tip sensor pose.

$$ {}^{OT}\boldsymbol{R}_{TipS(corr)} = \left({}^{OT}\boldsymbol{R}_{ShaftS(meas)}\right)^{-1} \cdot {}^{OT}\boldsymbol{R}_{ShaftS(calib)} \cdot {}^{OT}\boldsymbol{R}_{TipS(meas)} \tag{2.24} $$

$$ {}^{OT}\vec{\boldsymbol{t}}_{TipS(corr)} = -{}^{OT}\vec{\boldsymbol{t}}_{ShaftS(meas)} + {}^{OT}\vec{\boldsymbol{t}}_{ShaftS(calib)} + {}^{OT}\vec{\boldsymbol{t}}_{TipS(meas)} \tag{2.25} $$

2.5.2 Model and Segmentation Based Approach

As the intrinsic and extrinsic parameters of our camera have been determined beforehand (for camera calibration see section 2.2.2), together with optical tracking of the laparoscope OT bodies we know the spatial location of the camera image plane. Obviously we may use information readily available from the camera image together with that spatial information, in order to improve tracking accuracy. We therefore try to extract the US probe tip edges from the camera image and from that build a transformation, that partially corrects the overlay error. Notably the overlay error includes various errors ranging from tracking to calibration error.

We borrow some approaches, that already show promising results for application under conditions close to real laparoscopic conditions: similar to Climent and Marés [10] and

Voros *et al.* [59, 60] we use an edge detection filter and a Hough transformation to extract edges from laparoscopic images. Also we use additional information to select candidate lines belonging to the transducer edges. Voros *et al.* and Doignon *et al.* [12] use information about the insertion points of laparoscopic instruments, because those stay relatively fixed during an intervention and can be used for segmentation of instruments. However, in our case the laparoscopic ultrasound transducer might be bent and then its edges are no more aligned with the insertion point, so we use tracking information about the tip sensor instead.

Robustness of our implementation's edge detection is surely inferior to those of other groups, but our focus was primarily on a proof of concept for extracting information for correction from the images, once the transducer has been successfully segmented.

Line extraction

We use the Open Source Computer Vision Library (OpenCV) library for image processing. First, we apply the Canny edge filter [8], then we extract all lines using a Hough transformation [1]. Both methods are provided by OpenCV and for each line we obtain the image coordinates of its two end points.

Line selection

For simplicity we do all computations in the camera coordinate frame, so the two-dimensional coordinates x_i and y_i of each end point get back-projected into the three-dimensional space as

$$K^{-1} \begin{bmatrix} x_i \\ y_i \\ 1 \end{bmatrix} = \begin{bmatrix} x_c \\ y_c \\ 1 \end{bmatrix} = \begin{bmatrix} x_c \\ y_c \\ z_c \end{bmatrix} = \boldsymbol{X}_C. \tag{2.26}$$

We may arbitrarily choose $z_c = 1$ in this equation as one representative of the resulting line.

When back-projecting lines into space (cf. figure 2.14), all resulting planes trivially contain the camera center, so each plane is completely defined by its normal vector. Given two back-projected end points $\boldsymbol{X}_{C_1}$ and $\boldsymbol{X}_{C_2}$, the normal vector n can be computed as

$$n = \frac{\boldsymbol{X}_{C_1} \times \boldsymbol{X}_{C_2}}{\|\boldsymbol{X}_{C_1} \times \boldsymbol{X}_{C_2}\|}. \tag{2.27}$$

The transducer tip axis is defined in tip sensor coordinates by the tip axis origin b_{TipS} and the tip axis direction d_{TipS} (for axis calibration see subsection 2.2.5) and both can be transformed into camera coordinates as

$$b_C = {}^C\boldsymbol{T}_{TipS} \cdot b_{TipS} \tag{2.28}$$

$$d_C = {}^C\boldsymbol{T}_{TipS} \cdot d_{TipS} \tag{2.29}$$

where the transformation ${}^C\boldsymbol{T}_{TipS}$ from the tip sensor coordinate frame to the camera coordinate frame can be obtained from optical tracking of the laparoscope and magneto-

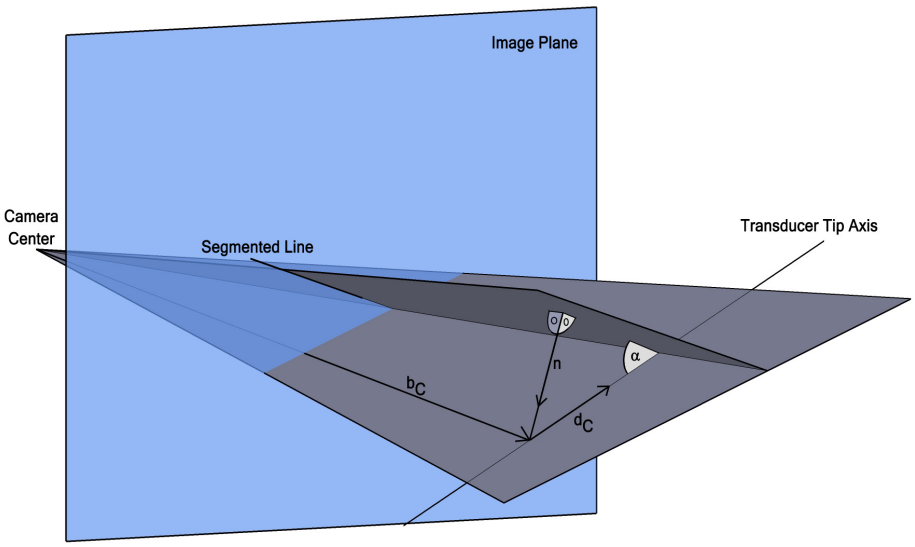

Figure 2.14: Back-projection of a segmented line and comparison to the transducer tip axis.

optic tracking of the tip sensor, favorably after applying the model based error correction (cf. section 2.3).

Both n and d_C are unit vectors, so the angle α between the transducer tip axis and the back-projected plane can be computed as

$$\|n\| \cdot \|d_C\| \cdot \sin(\alpha) \;=\; n \cdot d_C \tag{2.30}$$

$$\alpha \;=\; \arcsin(n \cdot d_C). \tag{2.31}$$

Similarly, the distance q of the calibrated tip axis origin b_C to the plane can be computed in the camera coordinate frame as

$$q = n \cdot b_C \tag{2.32}$$

This distance may be negative, so we can distinguish on which side of the plane the tip axis origin is.

Correcting transformation

Ideally, the back-projection of a segmented probe tip edge would yield a distance q from the tip axis of exactly half the probe diameter and an angle α of zero. For each line $|\alpha|$ and $|q|$ are compared to certain thresholds, e.g. we used thresholds $\alpha_{thresh} = 5$ (degrees) and $q_{thresh} = 30$ (millimeters), and we assume that the current line belongs to an edge of the US probe tip if both parameters are below the corresponding threshold.

Iterating over all lines belonging to the probe tip we store the minimum q_{min} and the maximum q_{max} of the distance q between the tip axis origin b_C and the back-projected plane. Ideally the difference between the minimum and maximum distance $|q_{max} - q_{min}|$ is equal to the diameter of the transducer tip. If the difference matches the diameter close

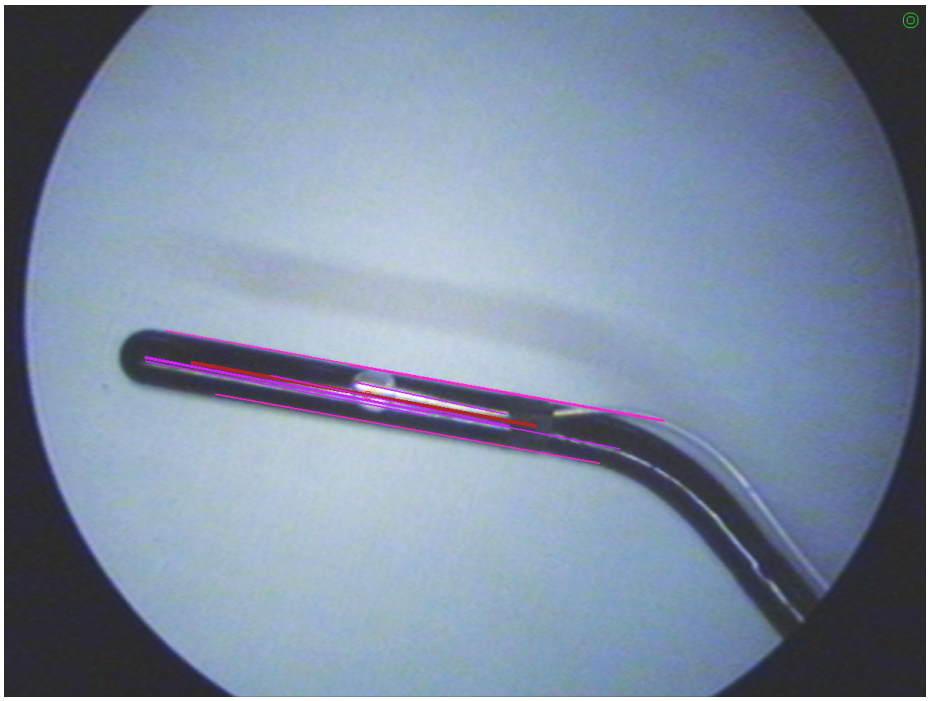

Figure 2.15: Screenshot of axis segmentation. Lines classified as belonging to the transducer tip edges are automatically colored pink, lines belonging to the transducer (but not the edges) are colored blue, the corrected transducer axis is thick red. Image brightness has been manually adjusted after taking the screenshot.

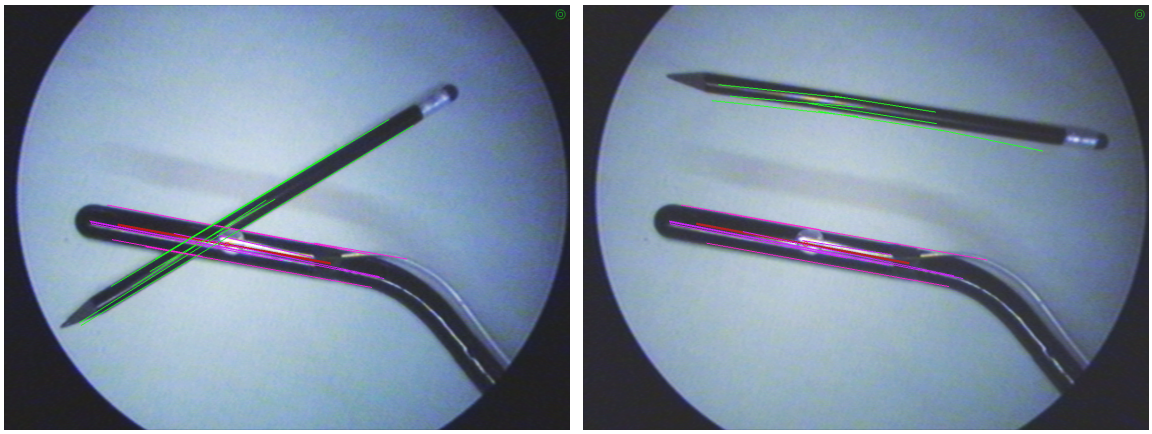

(a) (b)

Figure 2.16: Screenshot of axis segmentation. Lines along the pencil are rejected (colored green), because they do not match the measured transducer axis rotation (left) or location (right).

enough, say 10 ± 2 mm, we may assume that we have extracted lines belonging to each edge of the transducer.

We may assume that all those lines belong to a transducer edge whose distance only differs from either minimum or maximum by a certain threshold, e.g. two millimeters. Those $i = 1 \dots m$ lines are included in the further computation of the "mean plane normal"

$$\bar{n} \;=\; \frac{\sum_{i=1}^{m} n_i}{\| \sum_{i=1}^{m} n_i \|} \tag{2.33}$$

and the mean angle

$$\bar{\alpha} \;=\; \frac{1}{m} \sum_{i=1}^{m} \alpha_i. \tag{2.34}$$

The computation of $\bar{\alpha}$ is straightforward, but for $\bar{n}$ more sophisticated methods could be used. E.g. Kuffner [33] presents a set of algorithms for interpolation, that could be adapted to our needs, if necessary for future work.

The distance q_{corr} between the base point of segmented transducer axis and the measured transducer axis can be computed as the average of minimum and maximum distance

$$q_{corr} \;=\; \frac{1}{2} \left(q_{max} + q_{min} \right). \tag{2.35}$$

When translating the calibrated tip axis along the mean plane normal $\bar{n}$ by the supposed distance q_{corr}, the projected axis base point will be in the middle of the segmented probe tip. In a second step the axis is rotated into the back-projected plane: Since the rotation axis r has to be orthogonal to the plane normal as well as to the measured tip axis, we can compute it as $r = \bar{n} \times d_C$. Together with the mean angle $\bar{\alpha}$ between the calibrated tip axis and the plane, a correcting transformation can be computed: The translation component along the mean plane normal can be calculated as $q_{corr} \cdot \bar{n}$ and the rotation component can be computed from r and $\bar{\alpha}$ using Rodrigues' rotation formula[11]. This transformation maps the calibrated tip axis to a location and origin, from where it would be projected onto the image plane exactly coinciding with the segmented axis of the probe tip.

[11] Rodrigues' rotation formula gives an efficient method for computing the rotation matrix corresponding to a rotation by a certain angle about a fixed axis. Details can be found at e.g. `http://mathworld.wolfram.com/RodriguesRotationFormula.html`.

Experiments, Results and Discussion

3 Experiments and Results

The accuracy of our system is determined in two steps: first we assess the three-dimensional tracking accuracy of the system with and without our proposed error correction methods in comparison to a "Gold Standard" method (see below). Then, in a second step we measure the two-dimensional overlay accuracy in an application-specific setting, i.e. augmentation of a laparoscope camera image. Three-dimensional points can be projected onto the camera image plane, once the projective geometry of the camera is known. The overlay error is the difference between the computed two-dimensional location of the point in the image plane and the actual location as extracted from the video image.

Both steps cover different aspects: the tracking error is especially relevant for applications like three-dimensional US, while the overlay error additionally includes the camera calibration error and may be partially corrected using image segmentation technologies.

Our evaluation setup is depicted in figure 3.1. For evaluation we mounted an additional optical tracking (OT) body to the transducer tip ("tip OT body"). Then we determined the transformation ${}^{TipB}\boldsymbol{T}_{TipS}$ from the tip sensor to the tip OT (for hand-eye calibration see subsection 2.2.4) and used that together with OT as a "Gold Standard" method for determining the tip sensor pose. The term "Gold Standard" is commonly used for a method, that is known to have the highest possible accuracy. In our case, this method is not applicable in a clinical setup, because of the additional OT body at the tip, but we may use it for comparison of accuracy.

3.1 Ultrasound Calibration

Assessment of US calibration is only briefly covered in this thesis, as our main focus was on electromagnetic tracking (EMT). After acquiring 40 sensor poses and extracting the corresponding line parameters from the B-scan images, the calibration parameters are computed using the Levenberg-Marquardt algorithm (see subsection 2.2.1).

For verification a single insulated EMT sensor was submerged into the water bath and its tip was segmented manually in five regions of the B-scan image. This was repeated for four poses of the transducer, which were not used for the calibration. The sensor's position was transformed into the B-scan coordinated frame and the distance to the segmented position was computed.

In order to avoid misalignments of the sensor center with the center of the ultrasound beam, the sensor was kept parallel to the US plane and segmentation was only done, when the sensor was visible in the B-scan image to its greatest extent.

Those experiments were part of our previous work [17]. A root mean square (RMS) error of 1.69 mm, a standard deviation of 0.51 mm, and a maximum error of 2.39 mm could be obtained.

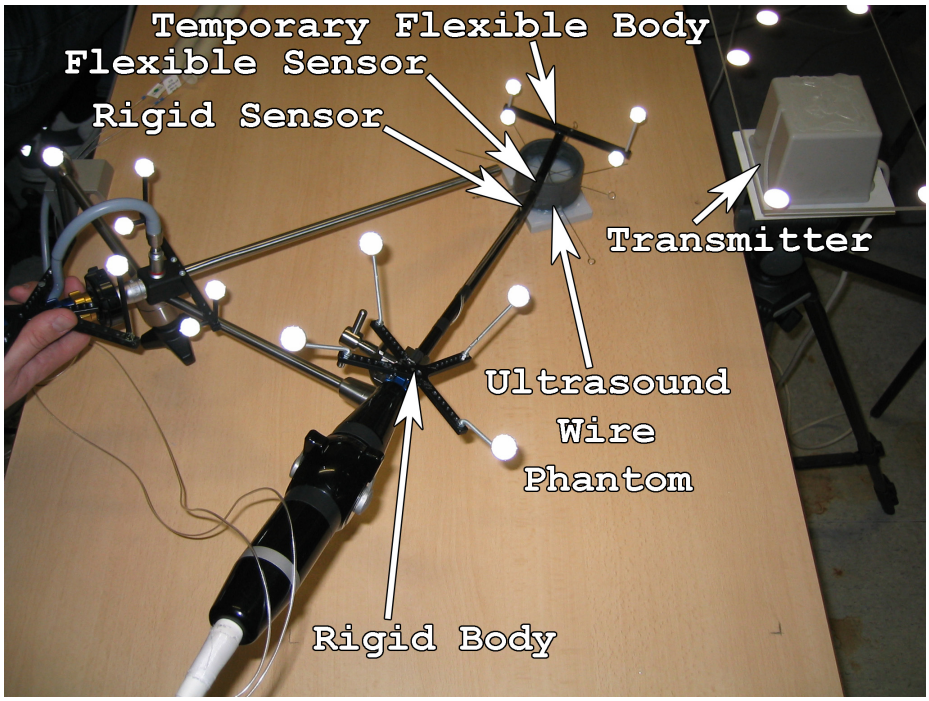

Figure 3.1: Evaluation setup. Note the temporary optical tracking body mounted at the transducer tip.

As attested by our collaborating surgeons, this error is acceptable under clinical conditions: In gastrointestinal[1] (laparoscopic) surgery conditions are different than in e.g. orthopedic surgery[2] or neurosurgery[3]. A discrimination of about 5 mm is usually sufficient for a number of reasons. Canalicular structures such as vessels, bile ducts, etc. play a critical role if they are equal to or thicker than 5 mm. Lymph nodes are considered to be inflicted by a tumor if the diameter is more than 10 mm and so on. Accordingly, this error of about 1.7 mm with a maximum error of 2.4 mm is certainly acceptable under clinical conditions.

3.2 Temporal Calibration

Temporal calibration of electromagnetic tracking reliably yields an offset of between 0.546 and 0.553 seconds for our setup, i.e. the electromagnetic tracking time stamps are approximately 55 ms behind the reference time. Unfortunately, values for temporal calibration of ultrasound imaging are not available.

[1] Gastrointestinal surgery is surgery of the digestive tract, i.e. stomach and intestines.
[2] Orthopedic surgery is surgery of the musculoskeletal system.
[3] Neurosurgery is surgery of the central and peripheral nervous system.

3.3 Axis Calibration

When doing axis calibration the RMS residual error of one calibration, i.e. the distance of the collected position measurements from the optimized cylinder surface, ranges from 0.57 mm to 1.03 mm with a mean value of 0.74 mm with model 130 sensors (six calibrations) resp. from 0.23 mm to 0.80 mm with a mean value of 0.42 mm with model 180 sensors (four calibrations).

3.4 Hand-Eye Calibration

When co-calibrating electromagnetic tracking (EMT) and optical tracking (OT) we determine the transformations ${}^{ShaftB}\boldsymbol{T}_{ShaftS}$ from the shaft EMT sensor to the shaft OT body and ${}^{TransB}\boldsymbol{T}_{EMT}$ from the EMT coordinate frame to the transmitter OT body. Because of tracking errors it is not possible to find an exact solution for both transformations, but only the optimal solution. At all poses, which were used for calibration, a root mean square (RMS) residual error of 1.29 mm for translation and 0.89 degrees for rotation remained after optimization. For detailed results before and after the optimization see table 3.1.

For verification we performed several subsequent calibrations. At least 13 poses of each calibration were used to verify the accuracy of the respective previous calibration. At each of these poses we computed the pose of both sensors by using either

1. We may take EMT measurements of the sensor's position relative to the EMT transmitter. Then we use the previously determined transformation ${}^{TransB}\boldsymbol{T}_{EMT}$ from the EMT coordinate frame to the transmitter OT body and optical tracking of the transmitter OT body to transform the sensor's coordinates into the OT coordinate frame (cf. equation 2.11, page 23).

2. The transformation ${}^{ShaftB}\boldsymbol{T}_{ShaftS}$ determines the position of the shaft EMT sensor relative to the shaft OT body. We may use this and optical tracking of the OT body to transform the sensor's coordinates into the OT coordinate frame (cf. equation 2.12, page 23).

The poses resulting from both methods were compared in translation and rotation, for results see table 3.2 (page 42). We computed the Euclidean distance in millimeters as translation distance, for rotation distance we computed the rotation between both poses, i.e. the rotation from one pose into the other, and used the rotation angle in degrees. Ideally both ways would yield identical poses for each sensor.

We performed two slightly different experiments: We measured the deviation during a calibration procedure (see above), i.e. the US probe was moved to different poses while the probe tip remained in an approximately neutral position, with only minor movements due to gravitational force. On the other hand, we fixed the probe in one position and moved the probe tip to all selectable positions using the levers. This was repeated for multiple other probe poses.

Additionally we measured the deviation at the shaft sensor, using the same techniques (for results also see table 3.2, page 42). The error at the shaft sensor is significantly higher than at the tip sensor. We largely, if not completely, attribute this to the larger distance

Before optimization	Min	Mean	Stdev	RMS	Max
Translation in mm	1.67	2.56	0.45	2.60	3.41
Rotation in degrees	0.56	1.04	0.18	1.06	1.44
δ	4.28	5.69	0.71	5.73	7.11

After optimization	Min	Mean	Stdev	RMS	Max
Translation in mm	0.33	1.19	0.48	1.29	2.05
Rotation in degrees	0.03	0.87	0.22	0.89	1.37
δ	2.12	3.79	0.70	3.85	5.70

Table 3.1: Hand-eye calibration residual errors before and after optimization. For the computation of δ see equation 2.13 (page 23).

between sensor and OT body: The mean orientation error for the shaft sensor error is 1.10 degrees. Obviously, this error only partly results in an additional position error, but for every 0.1 degrees it does, over the calibrated distance of 366 mm from the shaft sensor to the shaft OT body this amounts to an additional 0.6 mm of position error. At the tip sensor the same effect would only cause an additional 0.07 mm of position error, because the distance is smaller.

3.5 Modeling

When optimizing the model parameters, a residual error remains for the poses, that were used for computation (cf. section 2.3). For models determined from five pose sets the root mean square (RMS) error ranges from 3.48 to 3.89 degrees with mean 3.66 degrees for rotation and from 0.58 mm to 1.28 mm with mean value 0.94 mm for translation.

We assume the higher orientation error to be due to the fact that the bending region of our US probe proved to be not ideally elastic, i.e. a slight rotation around the instrument axis can still occur, which is not modeled by the current design. Especially when bending the transducer tip to extreme poses the pulling forces within the bending region could cause an additional rotation of the tip.

We verified the accuracy for another 171 poses, that were not used for computation (cf. figure 3.2). The rotation error stayed approximately the same (RMS was 3.22 degrees), but the translation error was higher (RMS 3.50 mm), especially for extreme poses, i.e. those with stronger bending of the transducer tip.

When optimizing the model for minimal difference to the measured tip sensor pose, the weighting of position difference in millimeters to orientation difference in degrees is 1:3 (cf. equation 2.13, page 23). The combined difference measure is dominated by the orientation difference, so poses with a smaller orientation difference are favored over those with a smaller position difference.

One possible solution might be choosing different weightings for the computation of the model parameters and for optimization for minimal difference to the measured tip sensor pose.

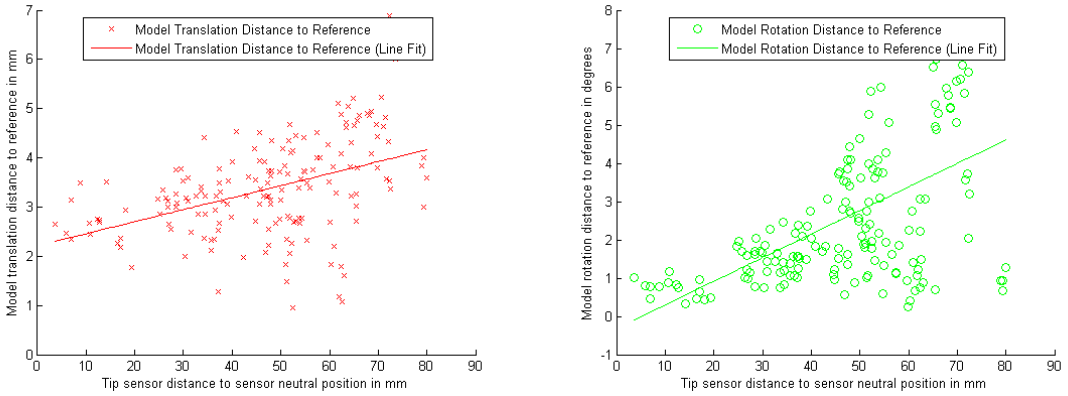

(a) (b)

Figure 3.2: Model errors, i.e. translation in millimeters (left) and rotation in degrees (right) in relation to the bending of the transducer tip, i.e. tip sensor distance to neutral position in millimeters.

3.6 Error Correction

When evaluating the hand-eye calibration performance, at the same time we evaluated the effectiveness of our proposed error correction.

For best possible comparison we assessed all errors simultaneously. We recorded 30 undistorted and 517 distorted measurements, applied both the shaft sensor based simple error correction (cf. subsection 2.5.1) and the model based error correction (cf. section 2.3), and recorded all distances to the reference pose, which was computed using the Gold Standard method.

For the model based error correction we used a weighting of position difference to the tip sensor pose in millimeters to orientation distance in degrees of 1:3 (cf. equation 2.13, page 23).

In the undistorted setting (see figure 3.3 and table 3.2) the tip sensor had a root mean square (RMS) error of 1.28 mm, the shaft sensor and the simple shaft sensor based error correction had an RMS error of 2.91 mm resp. 2.92 mm, and the model based error correction had an RMS error of 2.27 mm.

The simple shaft sensor based error correction performed almost exactly like the shaft sensor itself (for rotation it performed slightly worse). The model based error correction performed better, although it was anchored to the shaft optical tracking body and part of the corresponding hand-eye calibration error surely propagated into it.

Also in the distorted case (see figure 3.4 and table 3.3) the model based error correction with an RMS of 3.15 mm clearly outperformed the simple shaft sensor based approach with an RMS of 6.67 mm. Model based error correction proves functional, as the uncorrected tip sensor had an RMS of 6.91 mm. The orientation error, however, could not be improved (RMS 3.21 degrees uncorrected and 3.37 degrees corrected). This suggests that either the orientation difference to to the uncorrected sensor should be weighted stronger than it is now, or that the model needs to be extended to better approximate rotation of the

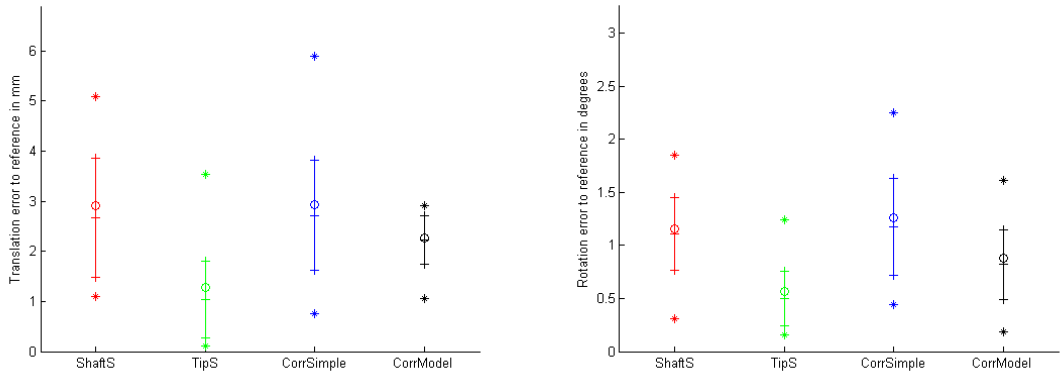

(a) (b)

Figure 3.3: 3D translation and rotation errors in an undistorted field. In each column, minimum and maximum are represented by a star, the RMS error by a circle, and mean and standard deviation by bars. For exact values see table 3.2.

Translation	Min	Mean	Stdev	RMS	Max
Shaft Sensor	1.10	2.66	1.19	2.91	5.09
Tip Sensor	0.10	1.03	0.77	1.28	3.54
Simple Correction	0.75	2.72	1.09	2.92	5.89
Model Based	1.06	2.22	0.48	2.27	2.90

Rotation	Min	Mean	Stdev	RMS	Max
Shaft Sensor	0.31	1.10	0.34	1.15	1.85
Tip Sensor	0.16	0.50	0.26	0.56	1.24
Simple Correction	0.44	1.18	0.46	1.26	2.25
Model Based	0.18	0.82	0.33	0.88	1.62

Table 3.2: 3D translation and rotation errors in an undistorted field. For a graphical comparision see figure 3.3.

transducer tip.

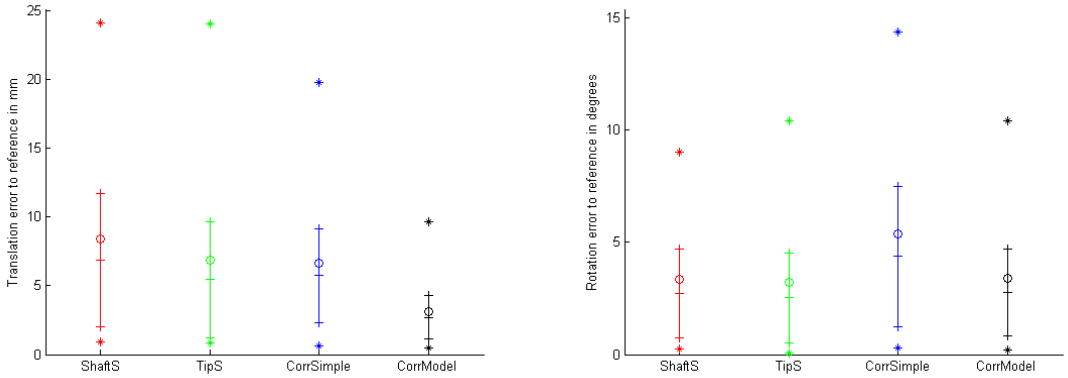

(a) (b)

Figure 3.4: 3D translation and rotation errors in a distorted field. The probe was fixed in varying locations and the electromagnetic field was distorted using either a knife, a steel rod, or a power supply unit. For exact values see table 3.3.

Translation	Min	Mean	Stdev	RMS	Max
Shaft Sensor	0.95	6.86	4.84	8.39	24.14
Tip Sensor	0.82	5.47	4.23	6.91	24.10
Simple Correction	0.59	5.73	3.42	6.67	19.85
Model Based	0.47	2.72	1.59	3.15	9.65

Rotation	Min	Mean	Stdev	RMS	Max
Shaft Sensor	0.25	2.71	1.99	3.36	9.01
Tip Sensor	0.08	2.52	1.99	3.21	10.40
Simple Correction	0.28	4.36	3.14	5.37	14.36
Model Based	0.18	2.77	1.93	3.37	10.38

Table 3.3: 3D translation and rotation errors in a distorted field. For a graphical comparision see figure 3.4.

For a comparison of both error correction approaches see figure 3.5. Whereas the simple shaft sensor based error correction had a much wider variance as well as a poorer overall performance, the model based error correction in most cases could reduce the translation error to below 5 mm, even for original errors up in the centimeter scale.

However, probably due to propagation of errors from tracking, calibration, and modeling, for errors lower than approximately 2.1 mm the model seems to give slightly worse results than the uncorrected tip sensor measurements. The model based error correction could thus be restricted to cases, where a relatively high error is predicted (for error prediction cf. section 2.4).

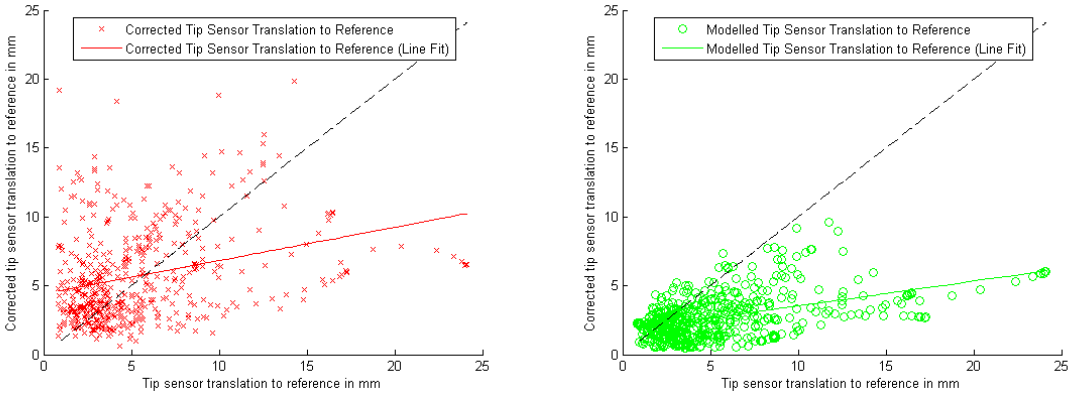

(a) (b)

Figure 3.5: Comparision of shaft sensor based error correction (left) and model based error correction (right) performance

3.7 Error Detection

We recorded 517 distorted measurements, using a knife, a steel rod with 10 mm diameter, and a power supply unit to create varying distortions of the electromagnetic tracking (EMT) field. For each measurement we computed the translation from the shaft sensor position (as measured via EMT, transmitter calibration, and optical tracking) to the shaft sensor reference position (as computed via hand-eye calibration and optical tracking), called "shaft sensor translation" below. We also computed the translation from the modeled tip sensor position (as computed via model based error correction) to the tip sensor position (as measured via EMT, transmitter calibration, and optical tracking), called "model-sensor translation" below. In an ideal and error-free setting both translations would be zero. Then both translation distances were each compared to the translation from the tip sensor position to the tip sensor reference position (as computed via hand-eye calibration and optical tracking), as illustrated in figure 3.6.

Both the shaft sensor translation and the model-sensor translation correlate with the tip sensor translation. As can be seen from figure 3.6, the shaft sensor translation is much more loosely correlated to the tip sensor translation (correlation coefficient is 0.69) than the model-sensor translation (correlation coefficient 0.95).

For both shaft sensor translation and model-sensor translation we can choose a threshold value, and predict a distortion of the tip sensor's pose, if the translation value is above the threshold.

Then two types of error in judgment are possible (explained for the shaft sensor based method, the model based follows accordingly): A false positive (type 1 error) occurs, when the distance between the calibrated pose and the measured pose is above the threshold, but the tip sensor measurement is actually not distorted, i.e. we erroneously reject data. A false negative (type 2 error) occurs, when the tip tracking is distorted, but the distance between both shaft sensor poses is below the threshold, i.e. we fail to predict the distortion. Note that the error in the hand-eye calibration is quite large (see section 3.4) at the shaft sensor,

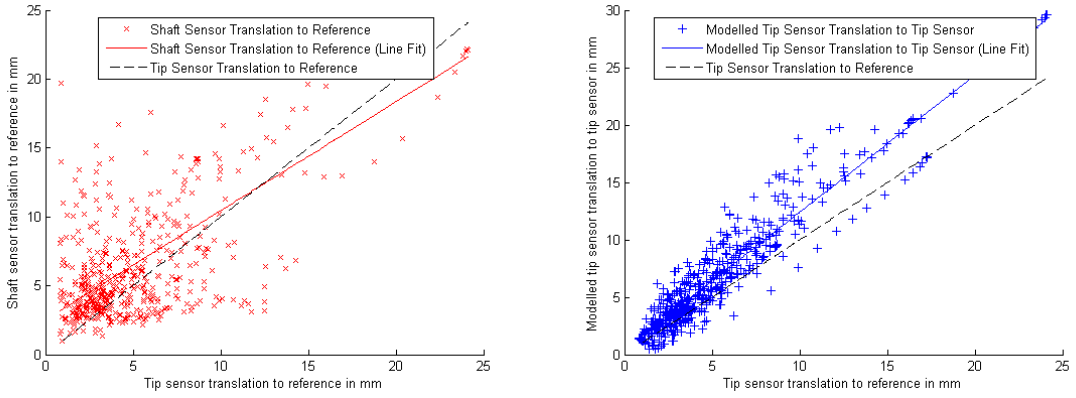

(a) (b)

Figure 3.6: Shaft sensor translation error (left) resp. translation of modeled tip sensor (right) to tip sensor, each in relation to the tip sensor translation to the tip sensor reference position.

so setting a low threshold value will likely trigger false positives. On the other hand we call correctly predicted errors "true positive" and correctly predicted absence of error "true negative".

For our set of distorted measurements we computed several Receiver Operating Characteristics (ROC) for predicting errors between 2.5 mm and 10 mm, i.e. how well both methods are able to predict erroneous measurements of the tip sensor position (see figure 3.7). Each point on the curve corresponds to a possible threshold value, and it displays the error ratios for the case if this value was used as threshold. We considered those values' performance as best, that yielded the maximum Youden index [63] when used as threshold value. The Youden index for a certain threshold is defined as follows:

$$J = \frac{ad - bc}{(a+b)(c+d)} \tag{3.1}$$

where a is the fraction of true positives, b the fraction of false negatives, c the fraction of false positives, and d the fraction of true negatives. The possible range of values is from zero to one inclusively.

In table 3.4 we present the key figures for each ROC: For both prediction methods the area under the ROC curve (AUC) and the maximum Youden index J_{max} have been computed. Additionally for the best threshold, i.e. the one with J_{max}, sensitivity and specificity and both the smallest false positive value FP_{min} and the greatest false negative value FN_{max} are given. The latter define the most extreme cases where the classifier would have made a wrong decision.

For predicting an error of 2.5 mm or greater, sensor based error prediction in the best case would have achieved a sensitivity of 50% and a specificity of 75%. That is, it would have been able to correctly predict 50% of all errors of 2.5 mm or greater and correctly predict 75% of those cases in our data set, where the error was below 2.5 mm. In comparison, the model based error prediction would have achieved a sensitivity of 91% and a specificity of

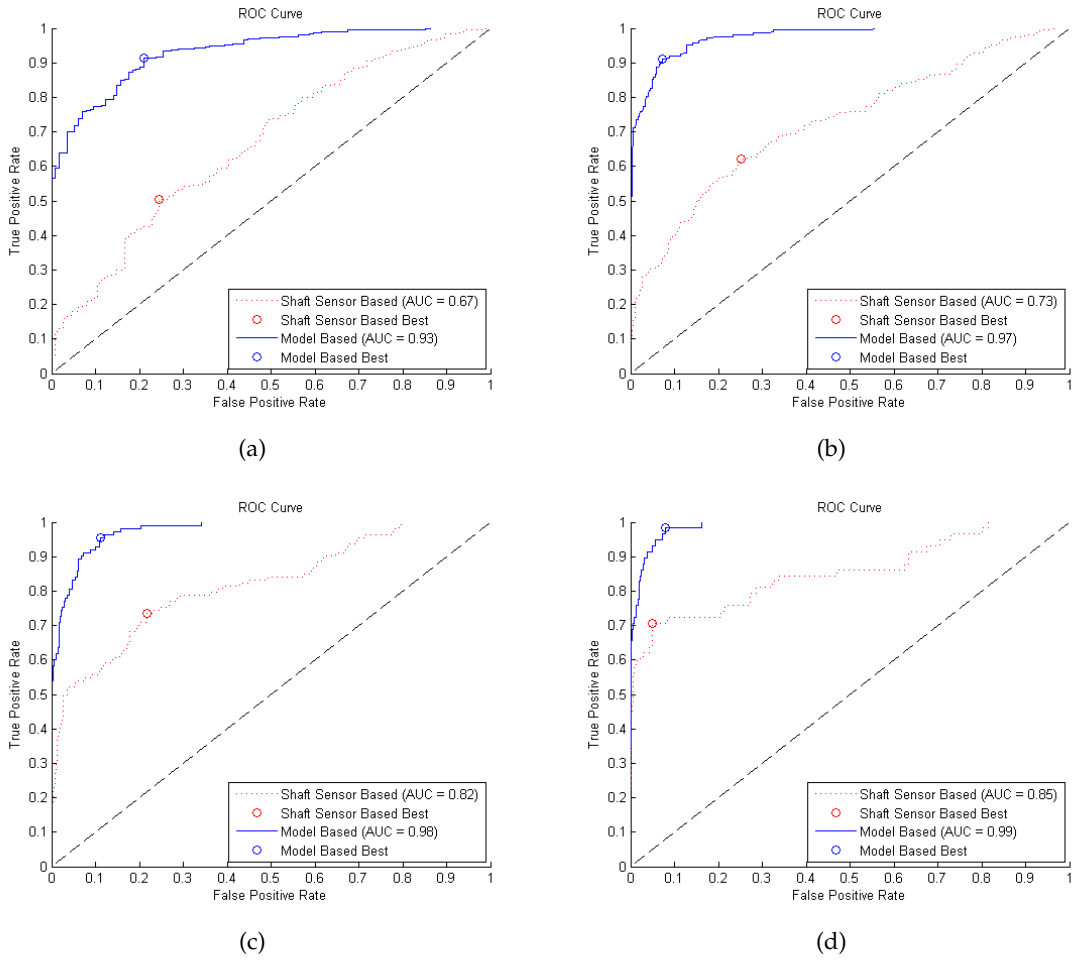

Figure 3.7: Receiver Operating Characteristics (ROCs) for 2.5, 5, 7.5., and 10mm

79% for the same data.

For predicting an error of 5 mm or greater, sensitivity and specificity would have been 62% and 75% (sensor based) resp. 91% and 93% (model based). For these values and those for 7.5 mm and 10 mm, see table 3.4.

The model based error prediction worked much more reliable. For example when predicting an error of 2.5 mm or greater it would have correctly predicted all good measurements better than 1.26 mm and all errors above 4.67 mm.

2.5 mm	AUC	J_{max}	Sensitivity	Specificity	FP_{min}	FN_{max}
Shaft Sensor Based	0.67	0.26	0.50	0.75	0.86	12.52
Model Based	0.93	0.70	0.91	0.79	1.26	4.67

5 mm	AUC	J_{max}	Sensitivity	Specificity	FP_{min}	FN_{max}
Shaft Sensor Based	0.73	0.37	0.62	0.75	0.86	12.52
Model Based	0.97	0.84	0.91	0.93	2.85	8.37

7.5 mm	AUC	J_{max}	Sensitivity	Specificity	FP_{min}	FN_{max}
Shaft Sensor Based	0.82	0.52	0.73	0.78	0.86	14.29
Model Based	0.98	0.84	0.96	0.89	4.64	9.93

10 mm	AUC	J_{max}	Sensitivity	Specificity	FP_{min}	FN_{max}
Shaft Sensor Based	0.85	0.66	0.71	0.95	0.88	14.29
Model Based	0.99	0.90	0.98	0.92	5.70	11.03

Table 3.4: ROC key figures

3.8 Overlay Accuracy

For assessing the overlay accuracy in both the undistorted and distorted case, the US transducer was fixed in various poses and the laparoscope was used to observe the transducer tip from various angles and distances between 5 cm and 20 cm. In the course of the experiments the transducer tip was steered to different angles and the laparoscope was also rotated around its own axis. For distorting the electromagnetic field we used the steel rod with 10 mm diameter again.

At each measurement

1. the uncorrected position of the tip sensor (“TipS”),
2. the shaft sensor based corrected position of the tip sensor (“CorrSimple”),
3. the model based corrected position of the tip sensor (“CorrModel”), and either
4. the segmentation based corrected position of the tip sensor (“CorrSegm”) or

5. a combination of 3 and 4 (instead of 4 only)

were transformed using the transformation ${}^{TipB}\boldsymbol{T}_{TipS}$ from the tip sensor to the tip optical tracking (OT) body. The resulting positions were then projected into the image plane, whose spatial location was known from camera calibration (cf. subsection 2.2.2). Also, the exact three-dimensional position of the OT body (centered in one of the markers) was projected into the image plane. The distance in millimeters within the image plane to the segmented midpoint of the OT marker was computed and taken as measure for overlay accuracy.

In our previous experiments [17] (see figure 3.8) we used the steel rod to create dynamic distortions, similar to surgical instruments, and a metal plate to create static distortions, similar to an operating room table. At the time of these experiments only the shaft sensor based error correction method was available and the results were not yet promising: For an undistorted environment the accuracy of the corrected sensor was sometimes poorer than the uncorrected tip sensor measurements. Dynamic distortions got worse in most cases, only static distortions could be partially corrected, but still errors in the centimeter range remained.

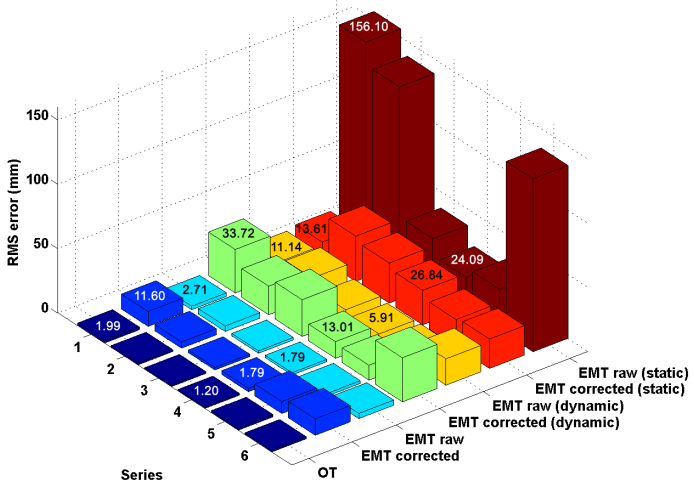

Figure 3.8: RMS projection errors. This figure has been taken from our previous work [17], only the shaft sensor based error correction was used in those experiments.

To assess the overlay accuracy of the new and improved error correction methods we took 207 undistorted and 935 distorted measurements. For the results in both undistorted and distorted case see figure 3.9 and table 3.5. As illustrated, the simple shaft sensor based error correction performed disappointingly also in the new 2D experiments, whereas the segmentation based error correction yielded minor improvements compared to the uncorrected tip sensor and the model based approach gained major improvements.

In figure 3.10 you can see a comparison of the error correction performance of

- the simple shaft sensor based error correction method,
- the model based error correction method, and

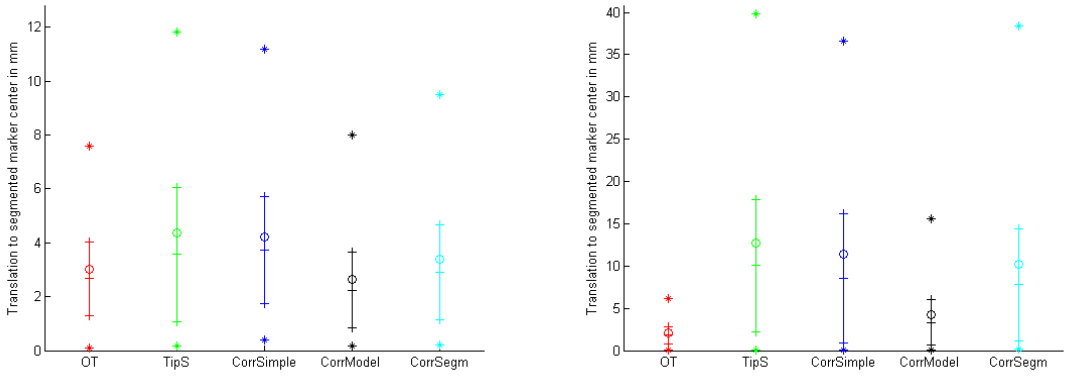

(a) (b)

Figure 3.9: Overlay errors in an undistorted and a distorted field. The model based and segmentation based method were not yet combined here.

Undistorted	Min	Mean	Stdev	RMS	Max
Projected OT	0.11	2.67	1.38	3.00	7.57
Projected EMT	0.17	3.57	2.49	4.35	11.81
Simple Correction	0.38	3.73	1.99	4.23	11.19
Model Based	0.15	2.25	1.39	2.64	7.99
Segmentation Based	0.20	2.91	1.75	3.39	9.51

Distorted	Min	Mean	Stdev	RMS	Max
Projected OT	0.05	1.81	1.02	2.08	6.10
Projected EMT	0.11	10.03	7.81	12.71	39.84
Simple Correction	0.07	8.55	7.63	11.45	36.66
Model Based	0.01	3.32	2.67	4.26	15.58
Segmentation Based	0.17	7.77	6.60	10.19	38.43

Table 3.5: Overlay errors in undistorted and distorted field

- the combined model and segmentation based error correction method.

Model based and segmentation based error correction can be combined to yield even better performance.

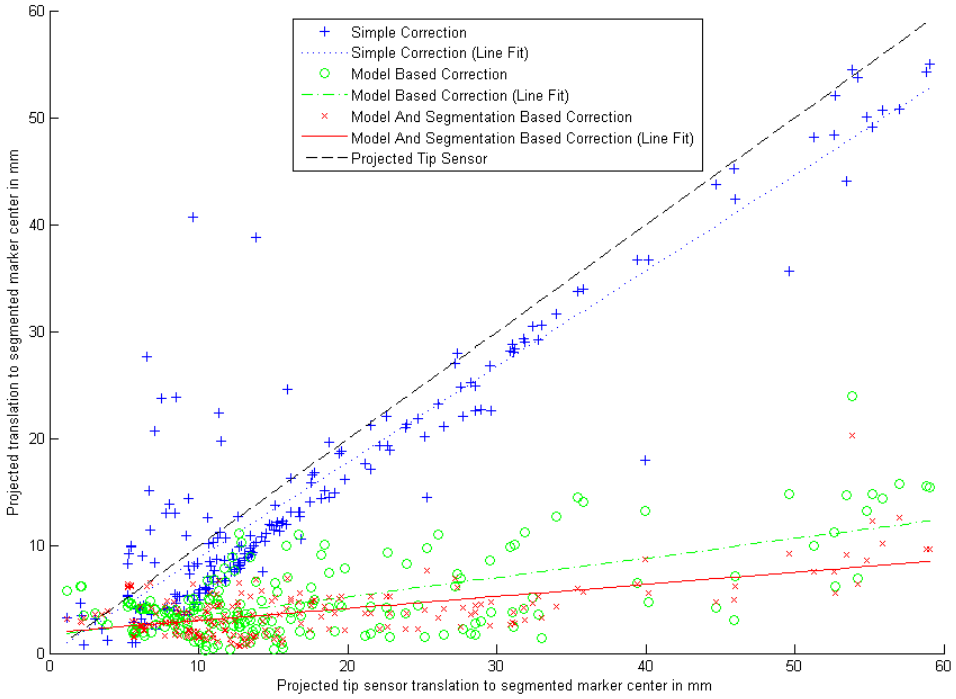

Figure 3.10: Performance of the different error correction methods. The model based and segmentation based methods have been combined.

4 Discussion

Our results show that the model based approach is clearly superior to the shaft sensor based method for error correction as well as for error detection. This chapter presents a comparison of our methods and results to related work. We investigate the differences and suggest possible directions for future research.

4.1 Error Detection

Birkfellner *et al.* [5] and Mucha *et al.* [41] already mentioned that the variation in field strength is usually not shift invariant, i.e. two sensors, mounted a certain distance apart, are affected differently by electromagnetic field distortions. While this is essential for their error detection methods, it significantly impacts our proposed shaft sensor based error detection and correction methods.

Both Birkfellner *et al.* and Mucha *et al.* fix two electromagnetic tracking sensors relatively to each other and to the electromagnetic tracking (EMT) transmitter. In a distortion-free environment Birkfellner *et al.* determine both sensors' correct positions and the distance between them. Mucha *et al.* do the same, but use the position of a calibrated pointer's tip, so they apply a rigid transformation to each sensor's pose before. Then both groups induce various distortions, measure one sensor's "movement" (its position is actually fixed) resp. the "movement" of the pointer's tip, and compare this to the measured deviation of the fixed distance between both positions.

The results of Birkfellner *et al.* are presented in table 4.1, where $\Delta_{det_{thresh}}$ is the threshold value for the deviation of the distance between both sensors. Using a threshold of 0.5 mm they were able to correctly detect 87% of all errors greater than 1 mm. Unfortunately they don't provide their ratio of false positives, so a direct comparison to our results is difficult.

$\Delta_{det_{thresh}}$	Detection rate (in %)
0.5	87
1.0	67
1.5	39
2.0	28

Table 4.1: Results by Birkfellner *et al.* [5]. "Detection rate" refers to the prediction of an error of more than 1 mm.

Mucha *et al.* used different instruments to induce distortions of the EMT field, as shown in table 4.2. For each instrument they present the correlation coefficient between the tracking error for the pointer's tip and the deviation of the distance p between both measurements. E.g. using forceps they caused a maximum tracking error p_{max} of 4.7 mm and the

correlation coefficient was 94%. Again, a direct comparison to our results is difficult given only the correlation coefficent.

Experiment	Correlation %	Maximum of measuring error p_{max} (mm)
Forceps	94	4.7
Shaver	80	8.7
Endoscope	49	1.1

Table 4.2: Results by Mucha *et al.* [41]

However, we may assume that our shaft sensor based error detection method performed similarly to the results of both Birkfellner *et al.* and Mucha *et al.*, although we faced additional difficulties: The distance between our shaft EMT sensor and the shaft optical tracking body is rather large (37 cm). This causes a hand-eye calibration error for the shaft sensor of 2.66 mm in our setup (see table 3.2, page 42), so low thresholds trigger false alarms easily. On the other hand, our setup had the advantage that the optical tracking of the shaft body is not affected by EMT field distortions.

In contrast to the shaft sensor based error detection, the model based approach clearly performs better than both Birkfellner *et al.* and Mucha *et al.*: We are able to achieve a higher sensitivity than Birkfellner *et al.* and a higher correlation than Mucha *et al.*.

Concerning applications in minimally invasive surgery, for the methods of Birkfellner *et al.* and Mucha *et al.* instruments with a rigid tip are required, where both sensors can be mounted. It would be possible to place two sensors at the tip of our transducer, but the distance between those must not be too small (Birkfellner *et al.* used 103 mm). Otherwise both sensors might in some cases be affected too similarly to reliably detect deviations.

4.2 Error Correction

The shaft sensor based error correction did not gain any improvements for the orientation error and only slight improvements for the position error. This suggests that tip sensor and shaft sensor are mounted too far apart to be affected by distortions, which are similar enough.

The model based error correction did reduce the position error from a root mean square (RMS) error of 6.91 mm to an RMS error of 3.15 mm. The orientation error stayed approximately the same (RMS 3.21° resp. 3.37°). The latter suggests that either the model should be refined to better match the real rotation, or that the rotation difference to the uncorrected tip sensor should be weighted stronger than it is now. However, there is a trade-off between orientation error and position error: A stronger weighting of the rotation difference to the uncorrected tip sensor can cause the model to favor poses with lower orientation error, but higher position error (cf. section 3.5). Finding an optimal combination surely requires further investigation.

To our knowledge no other method exists yet, that is capable of online error correction for the tracking of laparoscopic ultrasound and that does not need an on-site calibration of the tracking volume. Our proposed method only requires a single calibration, that can be done offline and remains valid for a long time, until the sensors are repositioned.

There might be limits to the achievable error correction capabilities of the model based approach: Errors are propagated and accumulated through tracking, hand-eye calibration, axis calibration, and modeling. Also, co-calibration introduces additional errors. Nakamoto *et al.* [45] mention that in their setup the co-calibration of EMT and optical tracking alone introduced 0.1-0.2 mm of additional error compared to using EMT only. Probably even higher errors have to be accepted for the calibration of the LUS probe shaft, because especially the shaft optical tracking body and sensor are mounted a long distance apart.

The flat table transmitter recently presented by Ascension is designed to overcome distortions from below the transmitter, e.g. caused by the operating room table. Due to its lower excitation in our setup it unfortunately performed worse than the mid-range transmitter. Bigger sensors could be used to improve accuracy but this would require bigger trocars. Using Ascension model 130 or model 180 sensors the total diameter of the probe could be kept below 12 mm (including sterile cover), so it still fits a regular trocar.

Using One Sensor Only

It is even possible to abandon the shaft sensor entirely: The tip optical tracking (OT) body is then also needed for construction of the model, but like now it can be removed afterward: After determining the transformation ${}^{TipB}\boldsymbol{T}_{TipS}$ from the tip electromagnetic tracking (EMT) sensor to the tip OT body, it is possible to compute the tip sensor movement in relation to the shaft OT body. Instead of using ${}^{EMT}\boldsymbol{T}_{TipS}$ and ${}^{EMT}\boldsymbol{T}_{ShaftS}$ the model would be constructed from ${}^{OT}\boldsymbol{T}_{TipB} \cdot {}^{TipB}\boldsymbol{T}_{TipS}$ and ${}^{OT}\boldsymbol{T}_{ShaftB}$. For axis calibration, however, a calibration phantom would have to be constructed, which allows axis calibration using OT instead of EMT.

In the same manner, error detection using the model based approach would be possible – without a second sensor and still with superior performance compared to the current state of art. It should be verified that those assumptions are correct and that our proposed methods also work without an additional shaft sensor.

A second possibility would be ${}^{OT}\boldsymbol{T}_{TransB} \cdot {}^{TransB}\boldsymbol{T}_{EMT} \cdot {}^{EMT}\boldsymbol{T}_{TipS}$ and ${}^{OT}\boldsymbol{T}_{ShaftB}$. For this method even the tip OT body is not needed any more. But then the determination of the transformation ${}^{TransB}\boldsymbol{T}_{EMT}$ from the EMT coordinate frame to the transmitter OT body would require an additional calibration phantom, because for hand-eye calibration one EMT sensor and one OT body must be fixed in relation to each other. In our opinion this approach would also be less favorable, because more tracking and calibration errors may be accumulated during the determination of the model parameters.

4.3 Future Work

Redundant tracking of the US transducer shaft could be used to compute a distortion correction function on the fly. This would be similar to Nakada *et al.* [43] and Wu and Taylor [61], but contrary to conventional techniques, that usually need to be performed again before each intervention.

Future work also should include a quantification of the robustness of the error correction methods proposed in this thesis, especially of the usability of our segmentation based

approach in a clinical application. A method using more sophisticated segmentation techniques could still use our method of determining the needed correction transformation for the instrument tracking.

4.4 Conclusion

We introduce two new methods to detect and partially correct static and dynamic electromagnetic field distortions online, i.e. intraoperatively, without the need for a precomputed distortion function. We apply it to a laparoscopic ultrasound transducer whose pose is determined by a hybrid magneto-optic tracking system.

Especially the novel model based approach improves the state of art [5, 41] for error detection and correction. The proposed method can be applied to a large set of procedures, where laparoscopic ultrasound or similarly constructed instruments are used, e.g. to operations of the liver, biliary tract, and pancreas.

Appendix

List of Figures

List of Tables

Bibliography

[1] Dana H. Ballard. Generalizing the hough transform to detect arbitrary shapes. *Readings in computer vision: issues, problems, principles, and paradigms*, pages 714–725, 1987.

[2] Donna J. Barbot, John H. Marks, Rick I. Feld, Ji-Bin B. Liu, and Francis E. Rosato. Improved staging of liver tumors using laparoscopic intraoperative ultrasound. *Journal of Surgical Oncology*, 64(1):63–67, 1997.

[3] Wolfgang Birkfellner. *Tracking Systems in Surgical Navigation*. PhD thesis, Department of Biomedical Engineering and Physics, General Hospital, University of Vienna, 2000.

[4] Wolfgang Birkfellner, Franz Watzinger, Felix Wanschitz, Georg Enislidis, Christian Kollmann, Dietmar Rafolt, Robert Nowotny, Rolf Ewers, and Helmar Bergmann. Systematic distortions in magnetic position digitizers. *Medical Physics*, 25(11):2242–2248, November 1998.

[5] Wolfgang Birkfellner, Franz Watzinger, Felix Wanschitz, Georg Enislidis, Michael Truppe, Rolf Ewers, and Helmar Bergmann. Concepts and results in the development of a hybrid tracking system for cas. In *Proc. Int'l Conf. Medical Image Computing and Computer Assisted Intervention (MICCAI)*, Lecture Notes in Computer Science, pages 343–351, 1998.

[6] Wolfgang Birkfellner, Franz Watzinger, Felix Wanschitz, Rolf Ewers, and Helmar Bergmann. Calibration of tracking systems in a surgical environment. *IEEE Trans. Med. Imag.*, 17(5):737–742, October 1998.

[7] S. A. Boppart, T. F. Deutsch, and D. W. Rattner. Optical imaging technology in minimally invasive surgery – current status and future directions. *Surgical Endoscopy*, 13(7):718–722, July 1999.

[8] John Canny. A computational approach to edge detection. *IEEE Trans. Pattern Anal. Machine Intell.*, 8(6):679–698, 1986.

[9] A.J. Chung, P.J. Edwards, F. Deligianni, and G.Z. Yang. Freehand cocalibration of optical and electromagnetic trackers for navigated bronchoscopy. In *Proceesings of Medical Imaging and Augmented Reality: Second International Workshop, MIAR 2004, Beijing, China, August 19-20, 2004.*, 2004.

[10] Joan Climent and Pere Marés. Automatic instrument localization in laparoscopic surgery. *Electronic Letters on Computer Vision and Image Analysis*, 4(1):21–31, 2004.

[11] K. Daniilidis. Hand-eye calibration using dual quaternions. *International Journal of Robotics Research*, 18:286–298, 1999.

[12] C. Doignon, F. Nageotte, and M. de Mathelin. Segmentation and guidance of multiple rigid objects for intra-operative endoscopic vision. In *Workshop on Dynamic Vision, European Conference on Computer Vision*, 2006.

[13] James Ellsmere, Jeffery Stoll, William Wells, Ron Kikinis, Kirby Vosburgh, Robert Kane, David Brooks, and David Rattner. A new visualization technique for laparoscopic ultrasonography. *Surgery*, 136:84–92, 2004.

[14] James Ellsmere, Jeffrey Stoll, David W. Rattner, David Brooks, Robert Kane, William M. Wells, III, Ron Kikinis, and Kirby Vosburgh. A navigation system for augmenting laparoscopic ultrasound. In *Proc. Int'l Conf. Medical Image Computing and Computer Assisted Intervention (MICCAI)*, pages 184–191, 2003.

[15] Raúl San José Estépar, Nicholas Stylopoulos, Randy E. Ellis, Eigil Samset, Carl-Fredrik Westin, Christopher Thompson, and Kirby Vosburgh. Towards scarless surgery: An endoscopic-ultrasound navigation system for transgastric access procedures. In R. Larsen, M. Nielsen, and J. Sporring, editors, *Proc. Int'l Conf. Medical Image Computing and Computer Assisted Intervention (MICCAI)*, volume 4190 of *Lecture Notes in Computer Science*, pages 445–453. Springer-Verlag, 2006.

[16] Marco Feuerstein. *Augmented Reality in Laparoscopic Surgery - New Concepts for Intraoperative Multimodal Imaging*. PhD thesis, Technische Universität München, 2007.

[17] Marco Feuerstein, Tobias Reichl, Jakob Vogel, Armin Schneider, Hubertus Feussner, and Nassir Navab. Magneto-optic tracking of a flexible laparoscopic ultrasound transducer for laparoscope augmentation. In *Proc. Int'l Conf. Medical Image Computing and Computer Assisted Intervention (MICCAI)*, 2007. To appear at Int'l Conf. Medical Image Computing and Computer Assisted Intervention (MICCAI).

[18] Suvranu Ganguli, Jonathan B. Kruskal, Darren D. Brennan, and Robert A. Kane. Intraoperative laparoscopic ultrasound. *Radiologic Clinics of North America*, 44:925–935, 2006.

[19] J. Harms, H. Feussner, M. Baumgartner, A. Schneider, M. Donhauser, and G. Wessels. Three-dimensional navigated laparoscopic ultrasonography. *Surgical Endoscopy*, 15:1459–1462, 2001.

[20] Richard Hartley and Andrew Zisserman. *Multiple View Geometry in Computer Vision*. Cambridge University Press, 2nd edition, 2003.

[21] Janne Heikkilä and Olli Silvén. A four-step camera calibration procedure with implicit image correction. In *Proc. IEEE Conf. Computer Vision and Pattern Recognition (CVPR)*, pages 1106–1112. IEEE Computer Society, 1997.

[22] Hippocrates. On the surgery. eBooks@Adelaide, University of Adelaide, South Australia, April 2007.

[23] HH Holm and B. Skjoldbye. Interventional ultrasound. *Ultrasound Med Biol*, 22(7):773–89, 1996.

[24] Po-Wei Hsu, Richard W. Prager, Andrew H. Gee, and Graham M. Treece. Rapid, easy and reliable calibration for freehand 3d ultrasound. Technical report, University of Cambridge, Department of Engineering, 2005.

[25] Po-Wei Hsu, Richard W. Prager, Andrew H. Gee, and Graham M. Treece. Rapid, easy and reliable calibration for freehand 3d ultrasound. *Ultrasound in Medicine & Biology*, 32(6):823–835, June 2006.

[26] J. Hummel, M. Figl, W. Birkfellner, M. R. Bax, R. Shahidi, C. R. Maurer, Jr., and H. Bergmann. Evaluation of a new electromagnetic tracking system using a standardized assessment protocol. *Physics in Medicine and Biology*, 51:205–210, 2006.

[27] J. Hummel, M. Figl, C. Kollmann, and H. Bergmann. Evaluation of a miniature electromagnetic position tracker. *Medical Physics*, 29:2205–2212, 2002.

[28] Johann B. Hummel, Michael R. Bax, Michael L. Figl, Yan Kang, Calvin Maurer, Jr., Wolfgang W. Birkfellner, Helmar Bergmann, and Ramin Shahidi. Design and application of an assessment protocol for electromagnetic tracking systems. *Medical Physics*, 32(7):2371–2379, July 2005.

[29] J. J. Jakimowicz. Intraoperative ultrasonography in open and laparoscopic abdominal surgery: an overview. *Surgical Endoscopy*, 20:425–435, March 2006.

[30] Volodymyr V. Kindratenko. A survey of electromagnetic position tracker calibration techniques. *Virtual Reality: Research, Development, and Applications*, 5(3):169–182, 2000.

[31] M. Kleemann, P. Hildebrand, M. Birth, and H. P. Bruch. Laparoscopic ultrasound navigation in liver surgery: technical aspects and accuracy. *Surgical Endoscopy*, 20:726–729, 2006.

[32] Jochen Krücker, Anand Viswanathan, Jörn Borgert, Neil Glossop, Yibin Yanga, and Bradford J. Wood. An electro-magnetically tracked laparoscopic ultrasound for multimodality minimally invasive surgery. In *Computer Assisted Radiology and Surgery (CARS)*, 2005.

[33] James J. Kuffner. Effective sampling and distance metrics for 3d rigid body path planning. In *Proc. IEEE Int'l Conference on Robotics and Automation (ICRA)*, volume 4, pages 3993– 3998, April 2004.

[34] Thomas Langø. *Ultrasound Guided Surgery: Image Processing and Navigation*. PhD thesis, Norwegian University of Science and Technology, 2000.

[35] Joshua Leven and et al. Davinci canvas: A telerobotic surgical system with integrated, robot-assisted, laparoscopic ultrasound capability. In *Proc. Int'l Conf. Medical Image Computing and Computer Assisted Intervention (MICCAI)*, 2005.

[36] Kenneth Levenberg. A method for the solution of certain problems in least squares. *Quarterly of Applied Mathematics*, 2:164–168, 1944.

[37] P. C. Li, C.Y. Li, and W.C. Yeh. Tissue motion and elevational speckle decorrelation in freehand 3d ultrasound. *Ultrason Imaging*, 24(1):1–12, 2002.

[38] Mark A. Livingston and Andrei State. Magnetic tracker calibration for improved augmented reality registration. *Presence: Teleoperators and Virtual Environments, MIT PressM*, 6(5):532–546, 1997.

[39] T. Mala and B. Edwin. Role and limitations of laparoscopic liver resection of colorectal metastases. *Digestive Diseases*, 23:142–150, 2005.

[40] Donald W. Marquardt. An algorithm for least-squares estimation of nonlinear parameters. *Journal of the Society for Industrial and Applied Mathematics*, 11(2):431–441, June 1963.

[41] Dirk Mucha, Bartosz Kosmecki, and Juergen Bier. Plausibility check for error compensation in electromagnetic navigation in endoscopic sinus surgery. *International Journal of Computer Assisted Radiology and Surgery*, 1:316–318, 2006.

[42] Christopher Nafis, Vern Jensen, Lee Beauregard, and Peter Anderson. Method for estimating dynamic em tracking accuracy of surgical navigation tools. In *Medical Imaging 2006: Visualization, Image-Guided Procedures, and Display*, 2006.

[43] Kazuhisa Nakada, Masahiko Nakamoto, Yoshinobu Sato, Kozo Konishi, Makoto Hashizume, and Shinichi Tamura. A rapid method for magnetic tracker calibration using a magneto-optic hybrid tracker. In Randy E. Ellis and Terry M. Peters, editors, *Proc. Int'l Conf. Medical Image Computing and Computer Assisted Intervention (MICCAI)*, volume 2879 of *Lecture Notes in Computer Science*, pages 285–293. Springer-Verlag, 2003.

[44] Masahiko Nakamoto, Hiroaki Hirayama, Yoshinobu Sato, Kozo Konishi, Yoshihiro Kakeji, Makoto Hashizume, and Shinichi Tamura. Recovery of liver motion and deformation due to respiration using laparoscopic freehand 3d ultrasound system. In R. Larsen, M. Nielsen, and J. Sporring, editors, *Proc. Int'l Conf. Medical Image Computing and Computer Assisted Intervention (MICCAI)*, volume 4191 of *Lecture Notes in Computer Science*, pages 372–379. Springer-Verlag, 2006.

[45] Masahiko Nakamoto, Yoshinobu Sato, Masaki Miyamoto, Yoshikazu Nakamjima, , Kozo Konishi, Mitsuo Shimada, Makoto Hashizume, and Shinichi Tamura. 3d ultrasound system using a magneto-optic hybrid tracker for augmented reality visualization in laparoscopic liver surgery. In *Proc. Int'l Conf. Medical Image Computing and Computer Assisted Intervention (MICCAI)*, 2002.

[46] Richard W. Prager, Andrew Gee, and Laurence Berman. Stradx: real-time acquisition and visualization of freehand three-dimensional ultrasound. *Medical Image Analysis*, 3(2):129–140, 1999.

[47] R.W. Prager, A.H. Gee, G.M. Treece, and L.H. Berman. Decompression and speckle detection for ultrasound images using the homodyned k-distribution. *Pattern Recognition Letters*, 24:705–713, 2003.

[48] R.W. Prager, R.N. Rohling, A.H. Gee, and L. Berman. Rapid calibration for 3-d freehand ultrasound. *Ultrasound in Medicine and Biology*, 24(6):855–869, 1998.

[49] Beate Rau, Michael Hünerbein, and Peter M. Schlag. Is there additional information from laparoscopic ultrasound in tumor staging? *Digestive Surgery*, 19:479–483, 2002.

[50] Francois Rousseau, Pierre Hellier, and Christian Barillot. Confhusius: A robust and fully automatic calibration method for 3d freehand ultrasound. *Medical Image Analysis*, 9:25–38, 2005.

[51] Yoshinobu Sato, Masaki Miyamoto, Masahiko Nakamoto, Yoshikazu Nakajima, Mitsuo Shimada, Makoto Hashizume, and Shinichi Tamura. 3d ultrasound image acquisition using a magneto-optic hybrid sensor for laparoscopic surgery. In W. Niessen and M. Viergever, editors, *Proc. Int'l Conf. Medical Image Computing and Computer Assisted Intervention (MICCAI)*, volume 2208 of *Lecture Notes in Computer Science*, pages 1151–1153. Springer-Verlag, 2001.

[52] Yoshinobu Sato, Masahiko Nakamoto, Yasuhiro Tamaki, Toshihiko Sasama, Isao Sakita, Yoshikazu Nakajima, Morito Monden, and Shinichi Tamura. Image guidance of breast cancer surgery using 3-d ultrasound images and augmented reality visualization. *IEEE Trans. Med. Imag.*, 17(5):681–693, 1998.

[53] J. Schmidt, F. Vogt, and H. Niemann. Robust hand-eye calibration of an endoscopic surgery robot using dual quaternions. In B. Michaelis and G. Krell, editors, *Pattern Recognition, 25th DAGM Symposium*, volume 2781 of *Lecture Notes in Computer Science*, pages 548–556, Berlin, Heidelberg, New York, 2003. Springer-Verlag.

[54] Tobias Sielhorst, Marco Feuerstein, Joerg Traub, Oliver Kutter, and Nassir Navab. Campar: A software framework guaranteeing quality for medical augmented reality. *Computer Assisted Radiology and Surgery (CARS)*, 1:29–30, 2006.

[55] Graham M. Treece, Andrew H. Gee, Richard W. Prager, Charlotte J. C. Cash, and Laurence H. Berman. High-definition freehand 3-d ultrasound. *Ultrasound in Medicine and Biology*, 29(4):529–546, 2003.

[56] R.Y. Tsai and R.K. Lenz. Real time versatile robotics hand/eye calibration using 3d machine vision. In *Proceedings of the IEEE International Conference on Robotics and Automation*, volume 1, pages 554–561, 1988.

[57] Theresa A. Tuthill, Jochen F. Krücker, J. Brian Fowlkes, and Paul L. Carson. Automated three-dimensional us frame positioning computed from elevational speckle decorrelation. *Radiology*, 209(2):575–582, 1998.

[58] Florian Vogt. *Augmented Light Field Visualization and Real-Time Image Enhancement for Computer Assisted Endoscopic Surgery*. PhD thesis, Universität Erlangen-Nürnberg, 2005.

[59] Sandrine Voros, Jean-Alexandre Long, and Philippe Cinquin. Automatic localization of laparoscopic instruments for the visual servoing of an endoscopic camera holder. In *Proc. Int'l Conf. Medical Image Computing and Computer Assisted Intervention (MICCAI)*, 2006.

[60] Sandrine Voros, Emmanuel Orvain, Philippe Cinquin, and Jean-Alexandre Long. Automatic detection of instruments in laparoscopic images: a first step towards high level command of robotized endoscopic holders. In *International Conference on Biomedical Robotics and Biomechatronics*, pages 1107–1112, February 2006.

[61] Xiaohui Wu and Russell Taylor. A direction space interpolation technique for calibration of electromagnetic surgical navigation systems. In Randy E. Ellis and Terry M. Peters, editors, *Proc. Int'l Conf. Medical Image Computing and Computer Assisted Intervention (MICCAI)*, volume 2879 of *Lecture Notes in Computer Science*, pages 215–222. Springer-Verlag, 2003.

[62] Tetsuzo Yamaguchi, Masahiko Nakamoto, Yoshinobu Sato, Kozo Konishi, Makoto Hashizume, Nobuhiko Sugano, Hideki Yoshikawa, and Shinichi Tamura. Development of a camera model and calibration procedure for oblique-viewing endoscopes. *Computer Aided Surgery*, 9:203–214, 2004.

[63] W. J. Youden. Index for rating diagnostic tests. *Cancer*, 3(1):32–35, 1950.

[64] Zhengyou Zhang. A flexible new technique for camera calibration. *IEEE Transactions on Pattern Analysis and Machine Intelligence*, 22(11):1330–1334, November 2000.